Ore-forming processes and mineral parageneses of the Jáchymov ore district

Rudotvorné procesy a minerální pragenze jáchymovského rudního okrsku

(77 figs, 6 tabs)

PETR ONDRUŠ[1] – FRANTIŠEK VESELOVSKÝ[1] – ANANDA GABAŠOVÁ[1] – MILAN DRÁBEK[1] – PETR DOBEŠ[1] – KAREL MALÝ[1] – JAN HLOUŠEK[2] – JIŘÍ SEJKORA[3]

[1] *Czech Geological Survey, Klárov 3, CZ-118 21, Prague 1*
[2] *U Roháčových kasáren 24, CZ-100 00, Prague 10*
[3] *National Museum, Václavské náměstí 68, CZ-115 79, Prague 1*

The contribution provides characteristics of the so-called *five-element* Ag–Ni–Co–Bi±U formation, points to differences in sources of the U formation and the Ag–Ni–Co–Bi–As formation, and presents a model of element fractionation in abyssal hydrothermal sources according to physical-chemical properties of the compounds. The role of arsine (AsH_3) in the mobility of the triad Ni–Co–Fe is discussed. A new scheme of mineralization stages is proposed in relation to three sources, separated in space and time: 1. greisenization of granite: *Sn–W sulpharsenide* stage. 2. U formation: *carbonate–uraninite* stage. 3. Ag–Ni–Co–Bi–As formation: *arsenide*, *arsenic–sulphide*, and *sulphide* stages. A new geochemical and thermodynamic interpretation of hydrothermal processes of individual mineralization stages is presented, including a detailed discussion of thermodynamic conditions of U^{VI} mobility and uraninite precipitation. Redox potentials of hydrothermal environment after the *carbonate–uraninite* stage including crystallization of silver and bismuth dendrites, precipitation of Ni–Co–Fe polyarsenides and electrochemical dissolution of Ag and Bi dendrites are also discussed. Mechanisms of the precipitation of base metal sulphides and sulpharsenides are considered in relation to redox conditions and sulphur fugacity in the environment during individual stages of mineralization. Phase relations are used for the deduction of the conditions of formation of selected ore minerals. Diagrammatic interpretation of chemical analyses and substitution trends of selected minerals or mineral groups, and a paragenetic relation of primary and secondary minerals are used in the interpretation. A discussion of the dependence of weathering processes on mining activity is included. Data on fluid inclusions and stable isotopes are used for the interpretation of ore-forming processes.

Key words: Ag–Ni–Co–Bi±U formation, mineralization stages, redox potentials, uraninite precipitation, Ag, Bi precipitation and electrodissolution, Ni–Co–Fe polyarsenides, fluid inclusions, stable isotopes, Jáchymov.

ELEMENT SOURCES AND FRACTIONATIONS

Mineralization sources

V. Zoubek suggests Proterozoic sediments containing local accumulations of uranium minerals as a source of U; the uranium is assumed to be released during the recrystallization of rocks (Štemprok 2003). Other hypothesis (Baumann et al. 2000) quote accessory minerals of granites as a uranium source; the release of uranium is associated with processes of metamorphosis of the host rocks in this case. Recent studies date the U-mineralisation as late-Variscan (i.e., Upper Paleozoic) – 300–240 Ma (Baumann et al. 2000), that means younger than greisens.

A connection of *five-element* mineralization to granites is assumed to be structural only instead of genetical (Baumann et al. 2000). Hence, the metals required were not released from granites but they came from unknown deep-seated sources and deposited in weakened structures that served also as feeder channels for granite intrusions. The feeder pathways for ore-forming solutions coincide with deep-seated faults of Gera-Jáchymov fault zone. The ore mineralisation resulted from post-Variscan tectonomagmatic re-activation which had a form of brittle tectonics. The mineralization is dated as post-Variscan (Mesozoic) with age 240–100 Ma.

Abyssal hydrothermal sources – a model for separation of elements

At least three independent thermal sources instrumental in the transport of ore-forming elements into the fractured crystalline complex and their accumulation are considered for the Jáchymov ore district.

1. The oldest thermal source is related to the intrusion of granite (Karlovy Vary pluton), underlying the complex of metamorphic rocks. Greisenization related to younger granite resulted in the enrichment of the apical parts of granite in Sn, W, As, S, Fe, Cu, (Mo, Cd, In), a.o.
2. The second source in the time sequence is responsible for the transportation of uranium in the form of uranyl-carbonate complexes into fractures in older granite and in the metamorphic complex. Information on the source of uranium is not available.
3. The youngest thermal source is responsible for the introduction of Ag–Ni–Co–Bi–As into pre-existing and partly mineralized open fractures. Hydrothermal fluids penetrated along fault zones from a crustal domain below the granite massif. The ultimate source of these elements is again unknown.

Fractionation of elements of the Ag–Ni–Co–Bi–As formation

Ag–Ni–Co–Bi–As formation

The character of the individual periods of mineralization is interpreted as a consequence of the fractionation of Ag, Bi, Ni, Co, Fe and As compounds in a 3D domain of an evolving hydrothermal system. The process includes repeated crystallization and selective separation of elements controlled by differences in physical-chemical properties of their compounds with non-metallic elements: S, As, Cl, F, O (Fig. 1).

Silver and bismuth are the first fractionated elements due to the volatility of Ag and Bi chloro-complexes in hydrothermal environment under elevated temperatures. The subsequent fraction contains Ni, Co, Fe bound in volatile complexes of the MeX_4 or MeX_6 type (where X = Cl, OH, H_2O and AsH_3). With regard to new data [578], separation of these elements by the formation of pentacarbonyl-like phases with ligand AsH_3, or substitution of AsH_3 for CO (e.g., phase as P analogue of $Fe(CO)_4(AsH_3)$ with dissociation energy of ca. 40 kcal/mol [578]) is possible. Other possible ligands are: N_2, CCH_2, CH_2, H_2, NH_3, PH_3 and many others. Evidence of the occurrence of $Ni(CO)_4$ in fermentation gases from a municipal sewage treatment plant was presented in [428].

This fraction is followed by a fraction containing only As(S) without significant metal concentration. In its final stages, these products were succeeded by the last fraction containing base metals (Pb, Cu, Zn, Fe) and S; arsenic content is insignificant.

The *five-element* association documented in the Jáchymov ore deposit with its succession of minerals corresponds to the outlined mechanism of element fractionation. The fact that certain minerals occur in several generations and in part in various oxidation states is interpreted as due to oscillating redox conditions and rejuvenations. For example, silver was primarily deposited as native metal, but was re-mobilized and deposited at other sites, under changed conditions, in the form of sulphides or sulphosalts.

PARAGENETIC RELATIONS OF THE ORE VEIN SYSTEM

Mineralization stages

Tectonic movements separated individual mineralization stages responsible for the deposition of the mineral contents of ore veins [374]. Deposition of vein minerals took place in several chemically specialized stages of mineralization. This development was accompanied by repeated opening of fractures and by fracturing of older vein minerals. Tectonization opened conduits for mineralizing solutions propagating along NW–SE-striking fault zones and lower-order faults. Tectonic effects accompanying the Tertiary volcanism included mainly movements on E–W-striking faults and the emplacement of basaltic breccia dykes. In places where ore veins were deformed by fault reactivation, their ore minerals were crushed and exposed

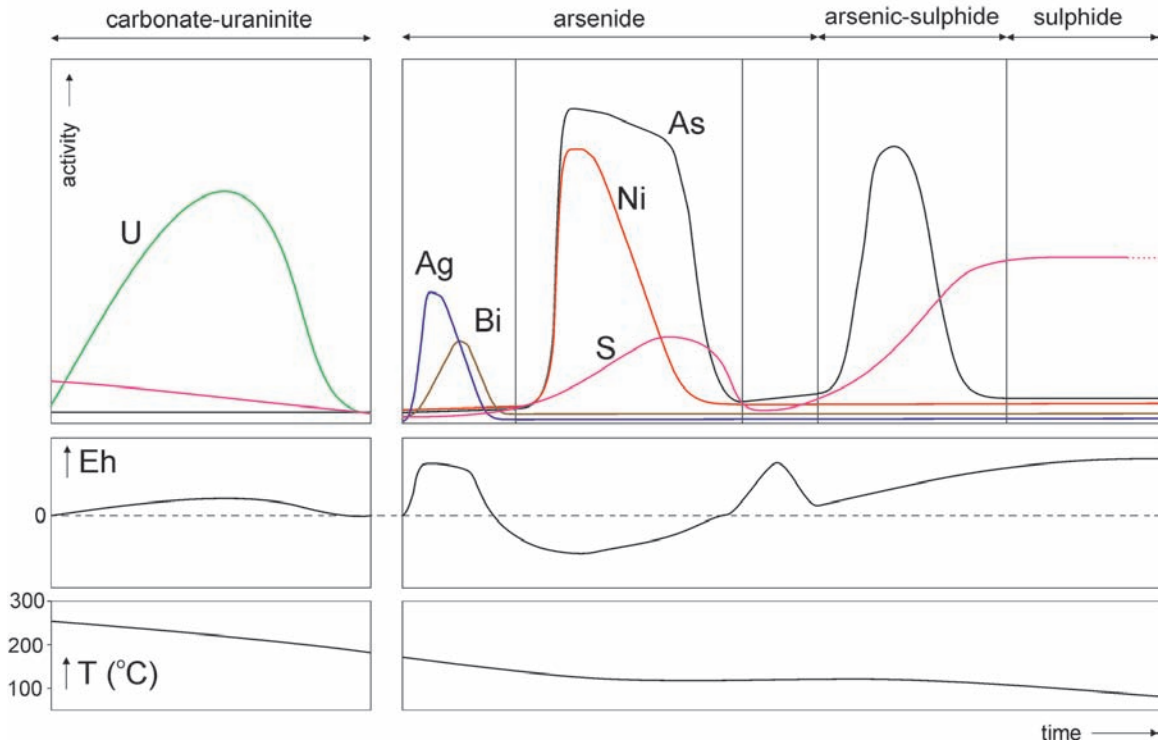

Fig. 1. Estimated trends of variation with time in activities of major elements, Eh and temperature during the main mineralization stages.

to enhanced groundwater flow, resulting in a stronger secondary alteration. The existing mineral filling of ore veins is not significantly complicated by tectonics post-dating the mineralization [374].

The complicated mineralization succession can be partly reconstructed only on the basis of the preserved information and material. The value of this information is weakened by the profound effects of the younger stages of mineralization. Only the middle and lower parts of the veins have been preserved, while the upper parts were removed by erosion.

The above complications affected the interpretation of mineralization stages and of sources of ore-bearing solutions, presented by various studies of the problem: [386], [431], [435], [436], [437], [438]. The time succession of mineralization stages proposed by Mrňa and Pavlů [351], [431], is presented here, modified with respect to the data of the present study.

Detailed characteristics of mineralization stages

Sn–W sulpharsenide stage

This stage is composed of several independent periods, which belong probably to high-temperature pneumatolytic and high-temperature hydrothermal mineralization stage known from Cínovec or from greisens of the Horní Slavkov–Krásno–Čistá area, also related to young granites. The authors of this study are convinced that this mineralization stage, or at least its younger period, is identical with the *older sulphide stage* defined by previous authors.

This stage of mineralization is probably the oldest one, with temperatures of ~300 °C (see *Fluid inclusion study*). The mineral paragenesis of *Sn–W sulpharsenide* mineralization is rare in the Jáchymov ore district. It was deposited on E–W structures, but the local characteristics of deposition are rather variable. It has been recorded in the Trojická vein, Svornost Shaft, Daniel level. In the Rovnost I mining field, minerals of this paragenesis are cut and displaced by about 0.5 m by veins of the *five-element* mineralization [431]. The Giftkies and No. 20 adits also encountered *Sn–W sulpharsenide* mineralization.

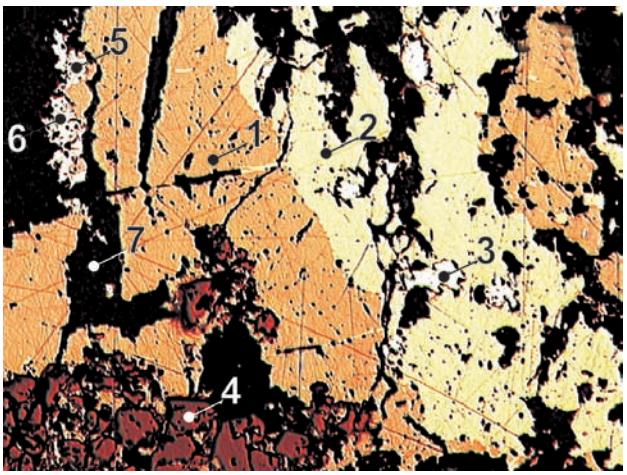

Fig. 2. J061P. Stannite replacing euhedral cassiterite is rimmed by chalcopyrite. Aggregate of intimate intergrowths of aikinite and matildite are at the left margin of stannite. Corroded arsenopyrite grains are enclosed in chalcopyrite. 1 – stannite, 2 – chalcopyrite, 3 – arsenopyrite, 4 – assiterite, 5 – aikinite, 6 – matildite, 7 – gangue. Adit No. 20. Reflected light, single polarizer. Magnification 65×.

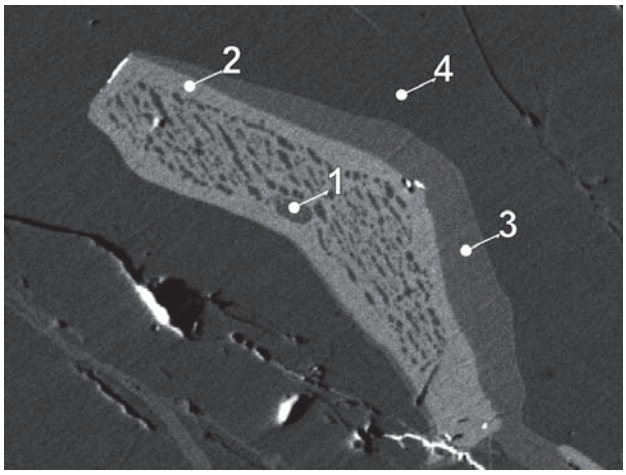

Fig. 3. J109P/2. 1 – covellite, 2 – stannite, 3 – bornite, 4 – chalcopyrite. Klement shaft. BSE image. Magnification 1150×.

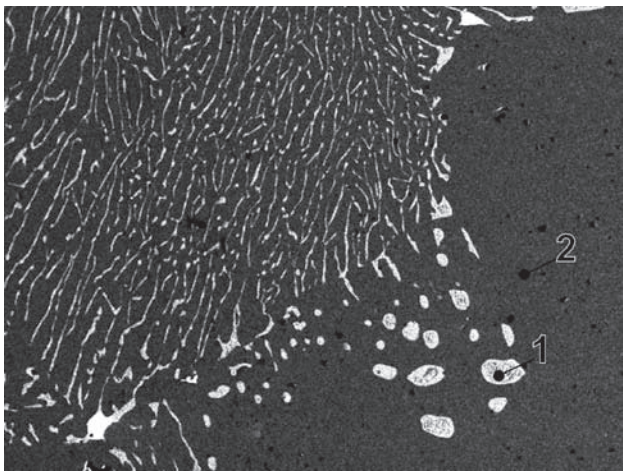

Fig. 4. J109P/3. 1 – stannite, 2 – chalcopyrite. Klement shaft. BSE image. Magnification 160×.

Minerals of this stage are not directly tied to the fracture system but represent accumulations in greisenized rocks. Rare and weak manifestations of this stage have been observed in some veins striking mainly NE–SW and E–W, e.g., Trojická vein. Principal minerals of this stage include *quartz, pyrite*, *arsenopyrite*, *tourmaline*, *phlogopite*, tungstenian *rutile*, *cassiterite* and *molybdenite* and younger sulphides: *chalcopyrite*, *bornite*, *tennantite*, *argentotennantite*, *freibergite*, *aikinite*, *matildite*, dark *sphalerite*, *galena*, *stannite*, *kësterite*, *mawsonite*, and *gersdorffite* (Figs 2–4). These minerals occur in *quartz* veins or as impregnations in strongly altered greisens, in various combinations or isolated.

Interesting is the accessory occurrence of microscopic *roquesite* enclosed in *mawsonite* and *stannite*, which indicate increased contents of In in the solutions. This points to a relationship of the Jáchymov *Sn–W sulpharsenide* stage with the closely similar paragenesis at Cínovec [448].

Ore-free quartz stage

This stage is characterized by various varieties of *quartz*, carbonates and rare *fluorite*. The oldest mineral is *quartz*, including chalcedony-like, ferruginous, amethystine quartz and quartz of pectinate texture. The grey chalcedony-like *quartz* carries inclusions of microscopic *pyrite* and clay minerals. Ferruginous *quartz* is brown red due to the pigmentation by Fe oxides and is locally impregnated by fine-grained *chalcopyrite*. Both types of *quartz* constitute characteristic vein filling of lower parts of the N–S veins. Pectinate *quartz* also widespread is either colourless or pigmented occasionally at crystal tips. It is deposited on fracture walls, fragments of wall-rock or on the breccia of the two above mentioned types of *quartz*.

Significantly less abundant are light green *fluorite* and (Fe,Ca)-carbonates, affected by replacement. In the interpretation by Dymkov [436], this stage would correspond to *quartz–fluorite* paragenesis, positioned at the beginning of the *carbonate–uraninite* stage.

Carbonate–uraninite stage

Products of this stage are present in variable quantities in a large number of veins striking NW–SE and N–S. Hydrothermal solutions of this period were moderately tempered near 200 °C, mineral paragenesis crystallized under moderately oxidizing, neutral, and weakly alkaline conditions, which varied considerably. Sulphur fugacity was low, locally increased SiO_2 activity resulted in the coffinitization of *uraninite*.

The main mineral is colloform, botryoidal *uraninite* accompanied by pink dolomitic carbonate, sporadic dark violet *fluorite*, grey to black *quartz* and *pyrite*. Radioactivity around *uraninite* aggregates turned *fluorite* to nearly black in colour. Carbonate crystals near *uraninite* contain thin layers rich in Fe oxides, indicating growth zones.

Uranium deposited as *uraninite* was repeatedly remobilized and participates in mineral paragenesis of nearly all mineralization stages.

Detailed characteristics of uranium mineralization

Uranium mineralization cemented fragments of the older *quartz* gangue, penetrated it in thin veinlets and, in other instances, formed with associated carbonates the sole thin veinlets filling. *Uraninite* usually formed monomineralic massive botryoidal aggregates only several cm thick, but extending for meters along the vein less frequently as short veins showing a symmetric structure. The associated gangue was *dolomite* or dolomitic carbonate, coloured in proximity of *uraninite* to creamy, buff pink or red. *Dolomite* is usually coarsely crystalline, coloured by Fe oxides.

Less common gangue minerals are *fluorite*, dark violet to black near *uraninite*. *Uraninite* was locally accompanied by *pyrite*, especially where dolomitic gangue was absent and *uraninite* was deposited directly in crushed and hydrothermally altered wall rock.

Uraninite mineralization often developed in significant concentrations, with *uraninite* prevailing over minerals of younger stages of mineralization. The original extent of uranium mineralization was larger than encountered during mining, since some parts of *uraninite* were replaced by hydrothermal solutions of the *arsenide* stage. *Uraninite* at Jáchymov has relatively high contents of REE. In the course of younger evolution of veins, several events of mobilization and regeneration of *uraninite* took place as indicated by the range of radiometric age determinations (see *Geology and hydrothermal vein system of the Jáchymov ore district*).

Other ore minerals, mainly arsenides, sulphides (dominantly *chalcopyrite* and *galena*), localized mainly in fractures of *uraninite* aggregates or at their margins, are younger than *uraninite* and belong to the paragenesis of later mineralization stages. Dymkov [436] considered that *calcite*, later subject to dolomitization, originally accompanied *uraninite*.

Arsenide stage

By volume, mineralization of the *arsenide* stage represents the major part of the total mineralization of the Ag-Ni-Co-Bi-As formation.

Successive relations among minerals of this stage are discussed by Keil [440], Dymkov [436], Zückert [423], Mrňa and Pavlů [351], [431] and others.

This stage is represented in a lower number of veins than uranium mineralization but is more varied and the most complicated in the district. It is characterized by low fugacity of sulphur and high fugacity of arsine. Hydrothermal mineralizing solutions were medium- to low-temperature, up to 200–250 °C, mineral assemblages crystallized in a strongly reducing, neutral or weakly acid environment.

The main gangue mineral is semitransparent or strongly pigmented *quartz* with frequent fine and dark grey ore impregnation. Arsenide ores are occasionally localized in

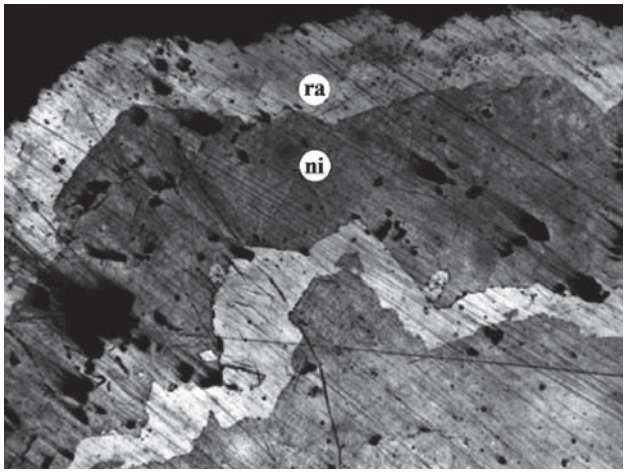

Fig. 5. Alternating layers of nickeline (ni) and rammelsbergite (ra). Svornost shaft, Geschieber vein. Magnification 83×. [524].

dolomitic carbonates. However, it is uncertain whether these carbonates belong to the *arsenide* stage or represent re-mobilized material from older vein filling.

In some cases, ore accumulations of diarsenides and triarsenides show features of a rapid growth under conditions of oscillating Ni/Co/Fe ratio. The mineralizing solutions were probably rather concentrated. A change in p-T conditions probably triggered the deposition of gel-like amorphous precipitates. A subsequent crystallization of such materials resulted in the formation of aggregates with contraction fractures filled by *quartz* or younger generations of ore minerals.

Crystals, if developed, are nearly always zoned *(nickel-skutterudite)*. Such changes are generally documented by repeated alternation of *nickeline* and *rammelsbergite* (Fig. 5) or by polymineral arsenide rim around *silver* or *bismuth*.

Primary *silver (bismuth)* crystals served as crystallization (nucleation) sites for arsenides and diarsenides.

The main part of ore minerals consists of *silver*, *bismuth*, *nickeline*, Ni–Co–Fe diarsenides *(safflorite, rammelsbergite, löllingite)* and triarsenides *(skutterudite, nickel-skutterudite)*. Minor aggregates of *uraninite*, remobilized from the uranium stage, represent a small heterogeneous component in the arsenide assemblage.

Arsenides are associated with alteration products of both native metals – regenerated *bismuth*, *bismuthinite*, *argentite*, *sternbergite*, *argentopyrite*, *silver*, a.o., less frequently alteration products of arsenides such as *gersdorffite*, *glaukodot*, *alloclasite*, *pararammelsbergite*, *krutovite*, a.o.

Several separate parageneses can be distinguished in the *arsenide* stage. Depending on the presence or absence of one of the two native metals, Ag and Bi, Zückert [423] introduced the following division:

Silver paragenesis

- *silver* + Ni arsenides – dendritic crystals of *silver* overgrown by *nickeline* and *rammelsbergite*. Exsolved *gersdorffite* has been occasionally observed.
- *silver* + *nickel-skutterudite* – crystals of native metal are surrounded by *nickel-skutterudite*, followed by younger *nickeline* and *rammelsbergite*
- *silver* + *rammelsbergite* + *safflorite* – larger-size *silver* dendrites are overgrown by a broader rim of *rammelsbergite*, coated by a thin layer of *safflorite*

Bismuth paragenesis

- *bismuth* + *safflorite* – skeletal *bismuth* crystals surrounded by *safflorite*
- *bismuth* + *skutterudite* – *bismuth* shapes depend on mutual ratio of both components in solution
- *bismuth* + Ni arsenides
- *bismuth* + *safflorite* + *rammelsbergite* – skeletal *bismuth* crystals are surrounded by thin *rammelsbergite* with a broader rim of *safflorite* or *safflorite–löllingite*
- *bismuth* + *safflorite* + *skutterudite* – unlike the association with *safflorite*, simple dendrites of *bismuth* are surrounded by *skutterudite* with a thin rim of *safflorite*
- *bismuth* + *löllingite* – *löllingite* forms thin rims on *bismuth*

Transitional paragenesis

- native Bi, *rammelsbergite*, *nickeline*

Arsenide paragenesis free of native metals

- *nickel-skutterudite*, *skutterudite*, *nickeline*, *löllingite*

Minerals of the bismuth paragenesis are more common than minerals of the silver paragenesis [383]. Both the parageneses often occur in the same vein or fracture filling but are sharply separated and form independent lenses. Common occurrence of *bismuth* and *silver* is exceptional in the form of irregular *bismuth* aggregates around *silver* dendrite. Krause [424] described vertical zoning in the Jáchymov veins, with predominance of *silver* in upper levels, gradually replaced by *bismuth* towards deeper levels.

The period of mineralization was probably of weak tectonic activity, and the flow velocity of the mineralizing solutions must have been very low as indicated by the presence of delicate and brittle aggregates including dendrites, skeletal or quill-like crystals.

Macroscopic description of mineral parageneses

A common feature of the parageneses is the presence of white isomorphous diarsenides and triarsenides constituting two series:

- anisotropic series: *rammelsbergite* $NiAs_2$ – *safflorite* $CoAs_2$ – *löllingite* $FeAs_2$
- isotropic series: *nickel-skutterudite* $NiAs_3$ – *skutterudite* $CoAs_3$

Ni–Co–Fe arsenides occur in the main paragenesis (i.e., *silver* and *bismuth*) as typical rims surrounding *silver* and *bismuth* (predominance of diarsenides), as well as independent grains and aggregates of variable shape. Most common are euhedral crystals – cubes of triarsenides, orthorhombic crystals of diarsenides, often in triplets having the shape of six-pointed stars.

The alternation of sharply defined layers is typical of polyarsenides (Fig. 5). The layers are often separated by a thin layer of remobilized *uraninite* of a younger generation.

The precipitation of polyarsenides took place in the succession:

arsenides ⇒ diarsenides ⇒ triarsenides,

and the oscillation in gradually increasing redox potential resulted in a partial repetition of the succession.

Silver paragenesis

This paragenesis includes ore minerals in dendrites forming mainly perimorphs after *silver*, which was largely dissolved during later hydrothermal processes. Resulting vugs and cavities were partly or completely filled with younger minerals, mainly ore-stage *quartz*, silver minerals (dominantly *argentite*) and sulphides. The main minerals of this paragenesis with Ni prevailing above Co are *nickel-skutterudite*, *rammelsbergite, nickeline*, rare *safflorite*, or *löllingite*.

Wire *silver* observed in occasional cavities does not belong to this paragenesis, since it was deposited later. Rather common is the alternation of thin botryoidal zones of *nickeline* with thicker layers of diarsenides and triarsenides. The precipitation of *nickeline* mainly occurred at an earlier time of the *arsenide* stage, with *nickeline* directly surrounding *silver* dendrites.

The analysis of minerals filling perimorphs of arsenides after *silver* indicates that *silver* was dissolved by solutions of the *sulphide* stage. The replacement of *silver* by diarsenides was not confirmed.

Dendrites with arsenide perimorphs after *silver* often reach the size of 5 cm and are hollow. The perimorphs were classified on morphological basis by Mrňa and Pavlů [383] as:

– dendrites with good crystal shape definition with branching corresponding to edges of cube (Fig. 6),
– dendrites well developed in one direction (Fig. 7),
– dendrites containing cavities which are imperfectly crystallographically defined (Fig. 8).

Bismuth paragenesis

Skeletal and quill-like *bismuth* crystals (Figs 9–10), often twinned, up to 2 cm long, are characteristic. Subhedral and irregular grains also occur. This paragenesis includes veinlets of younger *bismuth*, formed by the regeneration of primary *bismuth* and its deposition in fractures of gangue minerals. Owing to limited mobility of $BiCl_4^-$ complexes (liable to hydrolysis to BiOCl in slightly acid environment), the transport took place over the distance of several centimetres only.

Bismuth is common in paragenesis with arsenides containing increased Co and As, mainly *skutterudite*, *safflorite*, less frequently *löllingite*, *rammelsbergite* and *bismuthinite*. Such replacement is locally so intensive that perimorphs form. *Galena* and *sphalerite* are rimmed by a thin layer of *diarsenides* in the proximity of skeletal *bismuth*. *Nickeline*, typical of silver paragenesis, is rare in bismuth paragenesis. In a similar way as with silver dendrites, Ni–Co–Fe diarsenides form rims around skeletal *bismuth* crystals or fill cavities in *bismuth*. Unlike *silver*, *bismuth* may form lenses free of other ore minerals.

Analyses of ore lenses of bismuth paragenesis [351] show Ni : Co ratio up to 2 : 1, and cases of Co predominance occur. Notable is an increased As content in bis-

Fig. 6. Perimorphs of diarsenides of the 3rd generation (rammelsbergite, safflorite) after silver, quartz is black. Eliáš mine. Natural size. Mrňa and Pavlů [383].

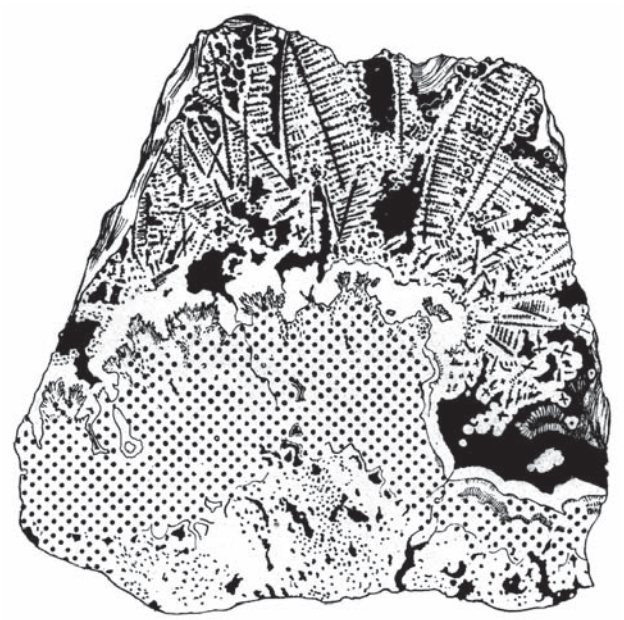

Fig. 7. Silver paragenesis, nickeline (stippled) is closely rimmed by white rammelsbergite of 2nd generation, in the upper part dendrites of diarsenides of the 3rd generation, quartz is black. Eduard shaft. Natural size. Mrňa and Pavlů [383].

Fig. 8. Silver paragenesis, thin rims of diarsenides coating cavities after silver, quartz is black. Eliáš mine. Natural size. Mrňa and Pavlů [383].

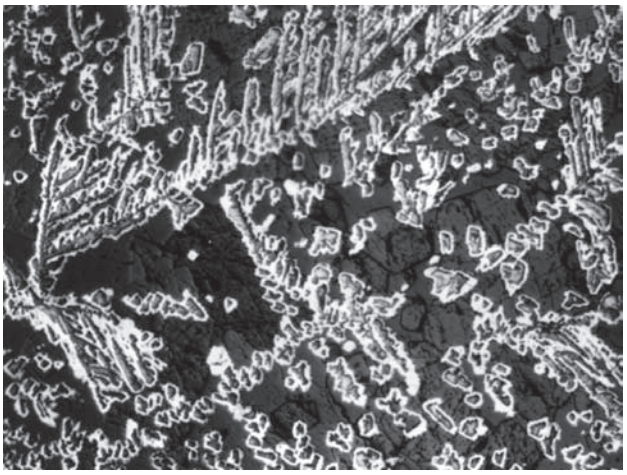

Fig. 9. Arsenide mineralization with bismuth. Svornost shaft, Geschieber vein. BSE image. Magnification 15×. [524].

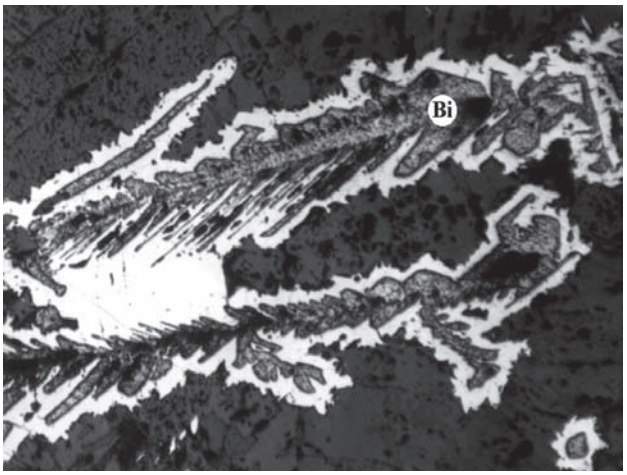

Fig. 10. Quill-like bismuth crystals rimmed by safflorite. Svornost shaft, Viktorie vein. BSE image. Magnification 65×. [524].

muth ores with Bi/As ratio of 1 : 2 to 1 : 2.8. In the silver paragenesis the Ag/As ratio is 1 : 1.5 to 1 : 2.3.

Mineral succession of the arsenide stage

The scheme of the precipitation succession of individual minerals of the arsenide stage is complicated by local physical and chemical conditions in a given part of the vein. The crystallization sequence is complicated by the superposition of a new generation of certain mineral and by the absence of some minerals in parts of the vein.

The compilation and evaluation of analytical and published data [351], [431] provided a basis for the scheme of mineralization succession in silver paragenesis of the *arsenide* stage:

ferruginous *quartz* ⇒ dendritic *silver* ⇒ spherulites of regenerated *uraninite* ⇒, *nickeline, nickel-skutterudite* (larger aggregates) ⇒ *rammelsbergite* (less frequently *safflorite*), *nickeline* ⇒ *rammelsbergite* (rimming *nickeline*) ⇒ *skutterudite* (mainly isolated crystals) ⇒ ore *quartz*, rare *carbonates*.

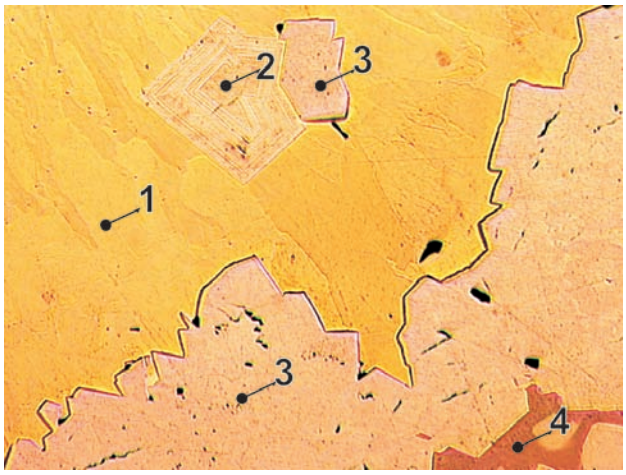

Fig. 11. J016P. Gersdorffite enclosed in radiating aggregates of nickeline. Rims of nickeline are formed by nickel-skutterudite with zonal texture and replaced by marcasite. 1 – nickeline, 2 – gersdorffite, 3 – nickel-skutterudite, 4 – marcasite. Bratrství shaft. Reflected light, single polarizer. Magnification 160×.

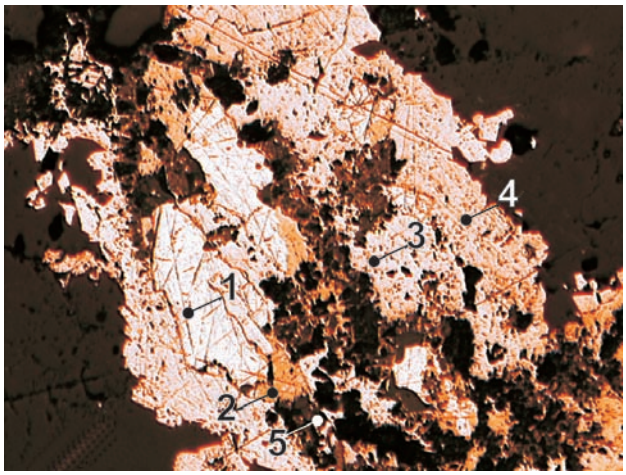

Fig. 12. J050P. Native bismuth on nickel-skutterudite is replaced by bismuthinite. Oval grains of uraninite at nickel-skutterudite-rammelsbergite contact. 1 – bismuth, 2 – bismuthinite, 3 – nickel-skutterudite, 4 – rammelsbergite, 5 – uraninite. Rovnost. Reflected light, single polarizer. Magnification 130×.

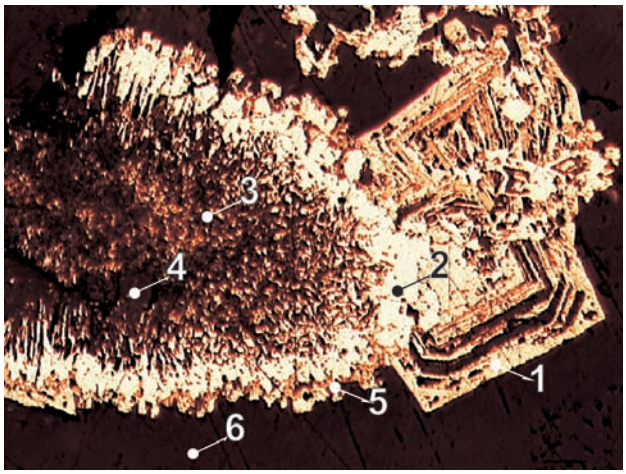

Fig. 13. J056P. Corroded cubic crystals of skutterudite grown on safflorite, which rims original rammelsbergite radial aggregates with centres of coffinitized uraninite. 1 – skutterudite, 2 – safflorite, 3 – rammelsbergite, 4 – coffinitizated uraninite, 5 – violarite, 6 – vein stuff. Svornost shaft, 5th level, Prokop(Co) vein. Reflected light, single polarizer. Magnification 130×.

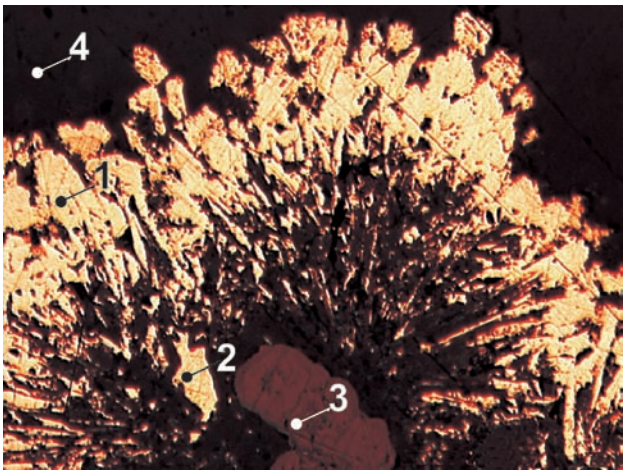

Fig. 14. J056P. Radial aggregates of acicular rammelsbergite enclose botryoidal uraninite, which is slightly coffinitized. Safflorite crystals grew on rammelsbergite. 1 – safflorite, 2 – rammelsbergite, 3 – uraninite and coffinite, 4 – gangue. Svornost shaft, 5th level, Prokop(Co) vein. Reflected light, single polarizer. Magnification 260×.

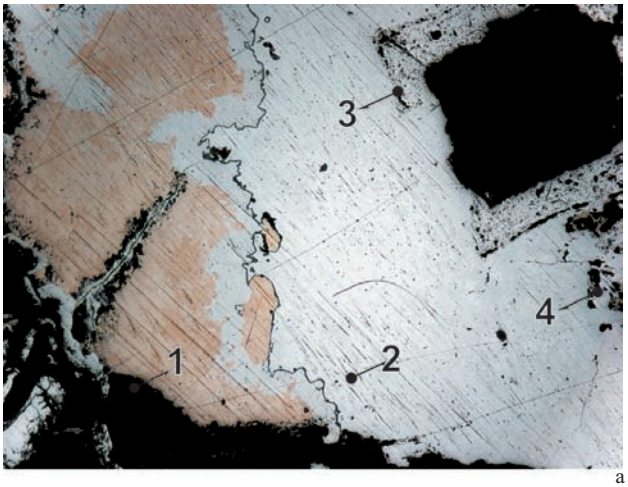

a

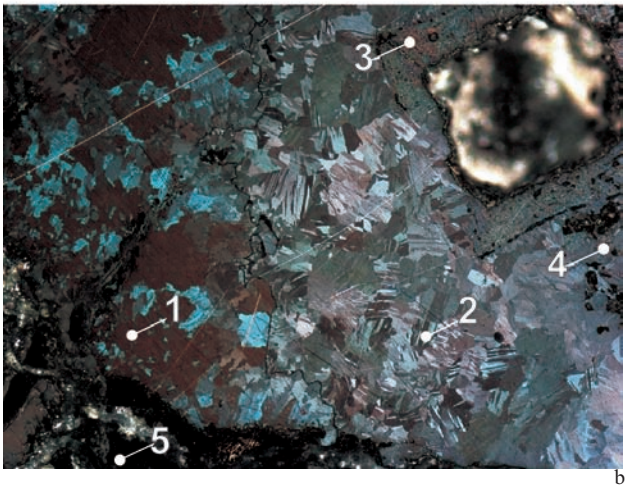

b

Fig. 15. J117P. The oldest nickel-skutterudite is corroded and dissolved and it is rimmed by rammelsbergite. The arsenides are in turn enclosed in zonal nickeline, which alternates with another generation of rammelsbergite. Border between monoarsenide and diarsenide is sharp. Chalcopyrite and proustite form minor inclusions near nickel-skutterudite. 1 – nickeline, 2 – rammelsbergite, 3 – nickel-skutterudite, 4 – chalcopyrite, nickelie 5 – carbonate. Eliáš mine, 2A vein. Reflected light. Magnification 100×.
a) single polarizer b) crossed polarizers

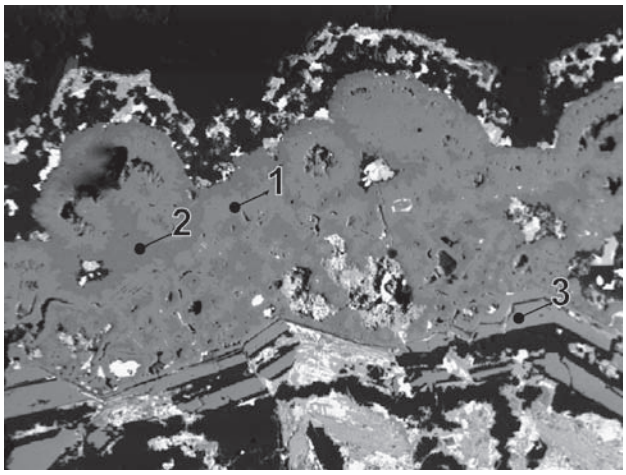

Fig. 16. MP290C/H-5. 1 – löllingite, 2 – gersdorffite, 3 – nickel-skutterudite. Barbora shaft, 5th level, vein No. 32. BSE image. Magnification 20×.

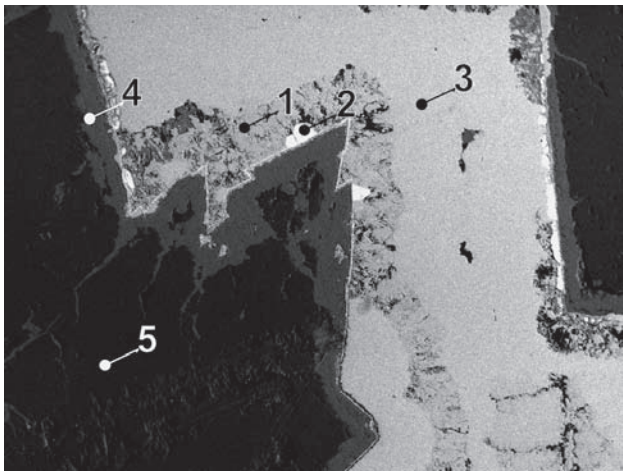

Fig. 17. MP511C/B-2. 1 – nickeline-(NAP), 2 – uraninite, 3 – rammelsbergite, 4 – annabergite, 5 – dolomite. Rovnost II shaft, 6th level, vein No. 16. BSE image. Magnification 60×.

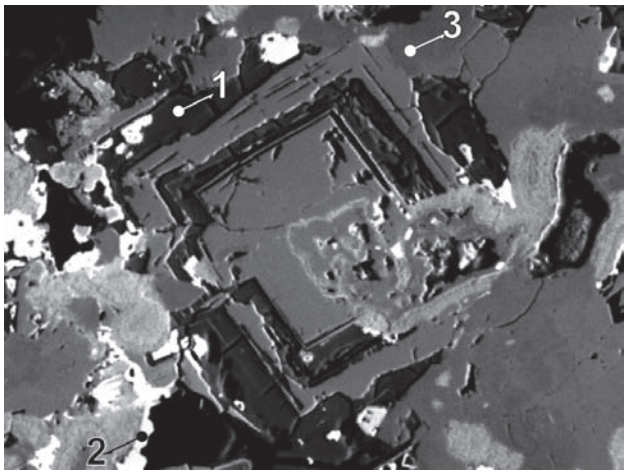

Fig. 18. J115P/B-1. 1 – arsenolite, 2 – matildite, 3 – nickel-skutterudite. Rovnost II shaft, 6th level, vein No. 16. BSE image. Magnification 800×.

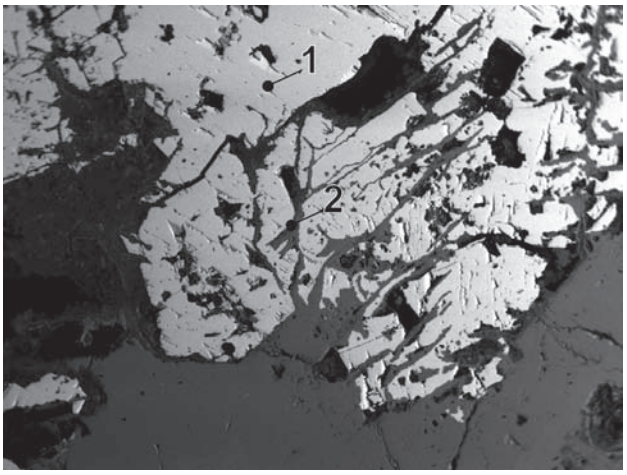

Fig. 19. J117P/A-8. 1 – galena, 2 – nickeline a rammelsbergite. Eliáš mine, 2A vein. BSE image. Magnification 16×.

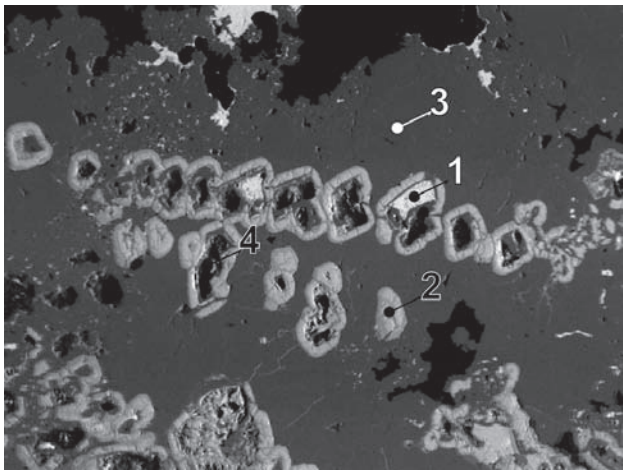

Fig. 22. MP215. 1 – bismuth, 2 – uraninite, 3 – rammelsbergite, 4 – perimorphs after silver. Tomáš shaft. BSE image. Magnification 100×.

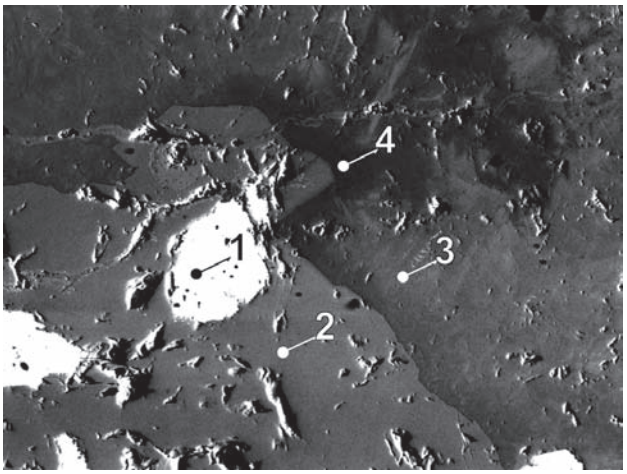

Fig. 20. J120P/B-1. 1 – bismuth, 2 – nickeline, 3 – rammelsbergite, 4 – S-rammelsbergite. Barbora shaft, 5th level, vein No. 32. BSE image. Magnification 130×.

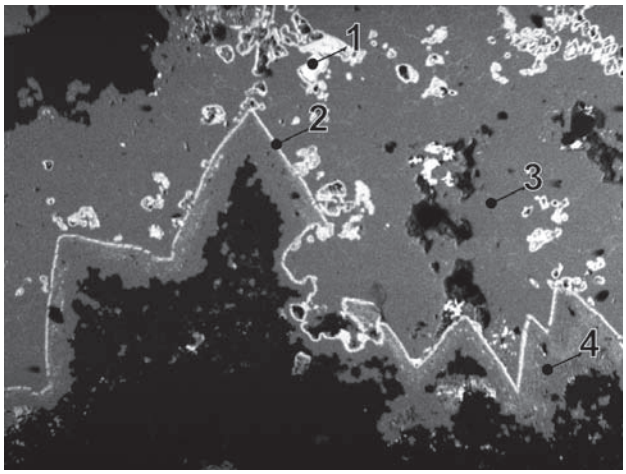

Fig. 23. MP215/1. 1 – bismuth, 2 – uraninite, 3 – rammelsbergite, 4 – nickel-skutterudite. Tomáš shaft. BSE image. Magnification 32×.

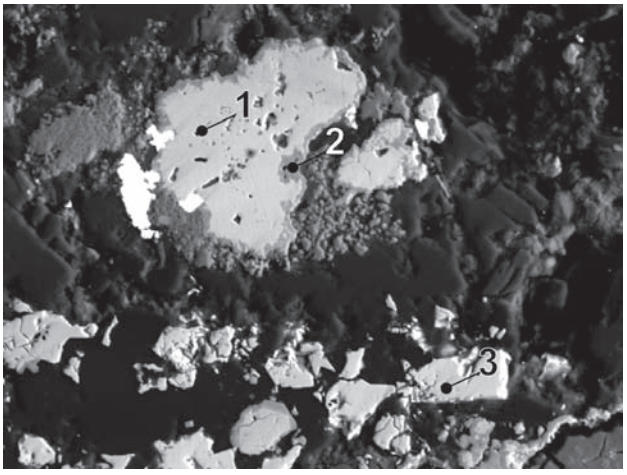

Fig. 21. MP41/D-2. 1 – rammelsbergite, 2 – Fe-gersdorffite, 3 – nickel-skutterudite. Svornost shaft, 10th level, Geschieber vein, BSE image. Magnification 750×.

The succession of the bismuth paragenesis is similar:

ferruginous quartz ⇒ *bismuth* ⇒ spherulites of regenerated *uraninite* ⇒ *skutterudite* (larger aggregates) ⇒ *safflorite* (or rare *rammelsbergite*) ⇒ *löllingite*, *skutterudite* (mostly colloform structures) ⇒ [*galena*, *sphalerite*] ⇒ ore *quartz*, rare carbonates.

Later or concurrently with the above-mentioned stages of arsenide mineralization, a number of other processes took place:

Native metals deposited as dendrites were partly or completely dissolved, *nickeline* was decomposed, secondary Bi and Ag minerals crystallized, precipitation of carbonates, *quartz* and copper minerals in vugs after leached native metals or among aggregates of arsenides took place. The basic scheme is complicated by "rhythmic" crystallization of arsenides (mainly *rammelsbergite, gersdorffite* and *nickeline*; Fig. 11), by several generations of regen-

erated *uraninite*, by the presence of younger dendritic *silver* deposited in sheaf-like aggregates on arsenides, the existence of several generations of *bismuth*, a.o. Other typical and characteristic minerals of this period are: *bismuthinite*, anhedral *bismuth*, *argentite* (Figs 11–23).

Arsenic–sulphide stage

Besides arsenic, sulphur and to some extent also antimony participated in the hydrothermal process of this mineralization stage. Typical is an increase in redox potential of ore-bearing solutions, neutral or weakly acid conditions and crystallization temperature in the range of 180–200 °C in early stages and ca. 60 °C in its closing stage.

This paragenesis occurs in numerous veins, particularly in the central and southwestern part of the district. The paragenesis occurs in a significant quantity and a wide vertical range in the Geschieber vein. Ores of this mineralization stage form either independent accumulations or associate with minerals of the *arsenide* stage, or with the youngest base metal *sulphide* mineralization stage.

The most common ore mineral is *arsenic*, accompanied by silver mineralization, sometimes with *realgar*, e.g., in the upper part of the Geschiber vein, and with *löllingite*. The main gangue mineral is dolomitic carbonate.

One of the oldest minerals of this stage is dendritic *silver* enclosed in lenses of *arsenic*. Leaching of silver or its substitution by *proustite* took place during this stage. *Silver* also occurs in globular aggregates directly in massive *arsenic*.

Silver paragenesis is represented by the following minerals: *Sb-proustite*, *As-pyrargyrite*, *stephanite* (important amounts in lower parts of the Geschiber vein), less frequent *argentite*, *pyrargyrite* (without *proustite*), *polybasite*, *arsenpolybasite*, *xanthoconite* and small crystalline aggregates or isolated crystals of *sternbergite* and *argentopyrite*. Silver is not represented to such degree as in the *arsenide* stage. Silver minerals of this paragenesis are dominantly deposited on *arsenic* or fill vugs in *arsenic*.

The single *arsenide* observed in silver paragenesis is *löllingite*, which rims *arsenic* aggregates in the form of small crystals.

In some important veins (Geschieber, Hildebrand), the *arsenic–sulphide* mineralization stage shows increased Sb contents which resulted in the following association of Sb minerals: *stibnite*, *pyrargyrite*, *antimony*, *dyscrasite*, *miargyrite*, *pyrargyrite*, *robinsonite*, *stibarsen*, and AsSb and BiSb inter-metallic phases. Mrňa and Pavlů [351] noted vertical zoning in Sb abundance in the Geschieber vein. It is demonstrated by the occurrence of Ag-sulphantimonates in lower levels, while in upper levels the content of Sb is lower, and Sb is contained mainly as equant admixture in *proustite*. *Pyrite* is also present in the above association of Sb minerals.

Sb facies of mineralization

Minerals containing Sb, or with prevalence of Sb above As, occur in the whole ore district, but are less numerous than minerals with prevailing As.

Sb is mainly contained in minerals of the *proustite–pyrargyrite* and *tennantite–tetrahedrite* series. It is impossible to identify crystallization sequence from the intergrowth of these minerals. In a similar way, relative succession cannot be determined from *tennantites* enriched in Sb. The presence of *tetrahedrite* filling fracture in *quartz* containing *tennantite* grains shows that *tetrahedrite* in the sample from Giftkies adit is younger than *tennantite*.

Sb content in *gersdorffites* is increased in late crystallization stages. In a similar way, Sb-*bismuthinite* crystallized in later stages.

The Hildebrand vein in the Svornost mine is known from historical records through the occurrence of Sb-bearing minerals. However, only a small number of precisely localized samples have been preserved from this fairly small vein, which occasionally yielded some good ores. The samples show that at least some parts of the vein reached notable enrichment in Sb, which enabled the origin of an anomalous mineral paragenesis for the Jáchymov deposit. *Antimony* was locally formed as inclusion in *miargyrite*, which is in equilibrium with Sb. Exceptionally, *pyrargyrite* occurs in this assemblage.

Arsenic also occurs in the paragenesis with Sb minerals. Its younger parts contain increased Sb contents of max. 7 wt. % and inclusions of *dyscrasite*. This situation indicates approximately the time interval in which the As-dominated evolution was terminated and succeeded by a phase with increased Sb concentration. Tectonic effects coinciding with the onset of this change are indicated by veinlets of younger *arsenic* filling thin fractures in coarse-grained *dolomite* and *calcite* in the proximity of older *arsenic*.

Obviously one of the youngest (in the stage) minerals is radiating *stibnite* resting on a band of botryoidal *pyrite* and enclosed in whitish *calcite*. Terminal parts of *stibnite* crystals are partly replaced by spheres of light yellow *sphalerite*. This indicates that Sb largely remained in solutions during the crystallization of ore minerals and increased in concentration during later stages.

Sulphide stage

Minerals of this stage are distributed fairly extensively, but the accumulations are minor, developed independently of older mineralization or deposited on older ores. Minerals of this stage fill contraction fractures in *uraninite* (*carbonate–uraninite* stage) and marginal, fractured, or leached volumes in ores of *arsenide* stage.

The main minerals are *galena* with a low Ag content, *sphalerite* (light with low Fe, In, Cd), *chalcopyrite*, *pyrite*, *marcasite* and sometimes *arsenopyrite*. Isolated finds include *bornite* with exsolved *chalcopyrite*, *boulangerite* and *tennantite*, accompanied by accessory *chalcopyrite*, *sphalerite* and *galena* [351] (Figs 24–32).

Predominant gangue mineral is *calcite*, containing impregnations of sulphides or alternating with sulphides in banded structures.

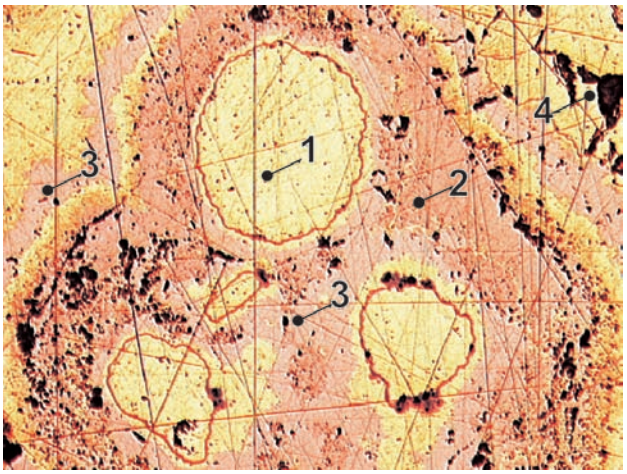

Fig. 24. J059P. Concentric aggregates of chalcopyrite alternate with tennantite. Rammelsbergite preserved in relics. As-chalcopyrite forms pink brown layers. 1 – chalcopyrite, 2 – tennantite, 3 – As-chalcopyrite, 4 – rammelsbergite, Svornosr shaft, 5th level, Prokop vein. Reflected light, single polarizer. Magnification 130×.

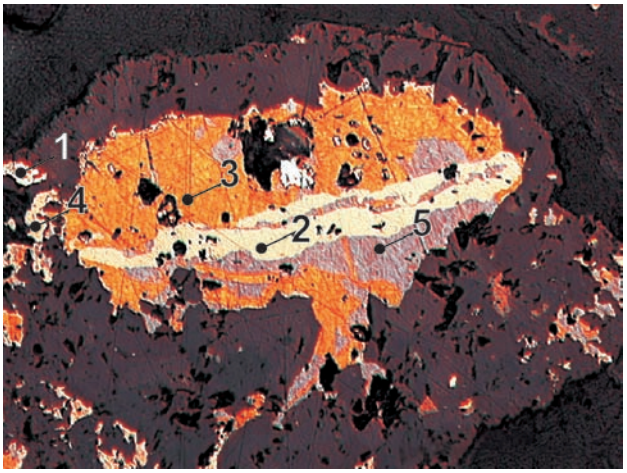

Fig. 25. Uraninite spherule enclosing rock fragment with relics of silver and fissure filled with chalcopyrite and bornite altered into covellite. Tennantite and silver in proximity. 1 – silver, 2 – chalcopyrite, 3 – bornite, 4 – tennantite, 5 – covellite. Svornost shaft, Daniel level, Trojická or Prokop vein. Reflected light, single polarizer. Magnification 260×.

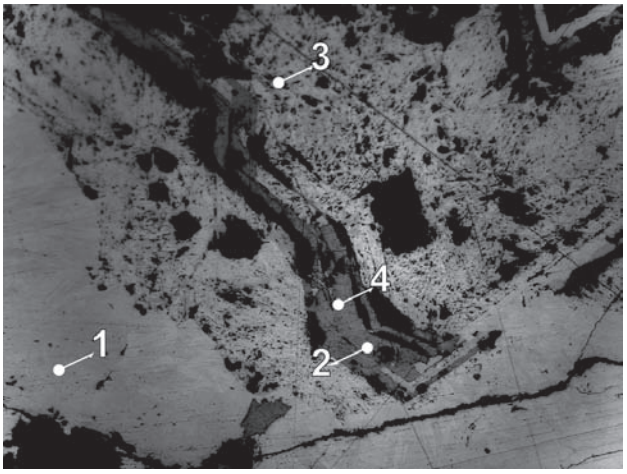

Fig. 26. J117P. 1 – rammelsbergite, 2 – chalcopyrite, 3 – nickel-skutterudite, 4 – argentite. Eliáš mine, 2A vein. Reflected light, single polarizer. Magnification 100×.

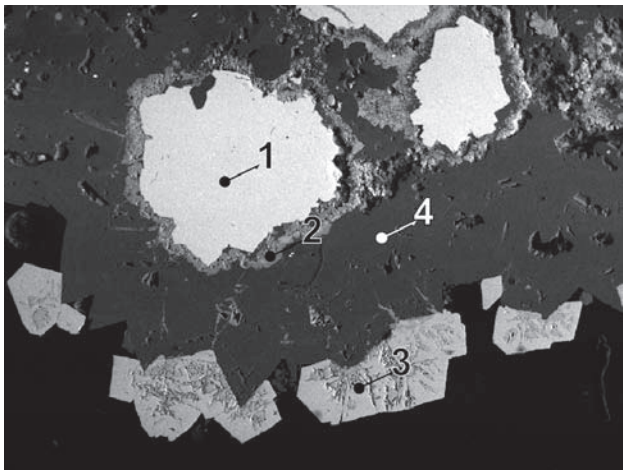

Fig. 27. J183P/4. 1 – sphalerite, 2 – pyrite, 3 – smythite and pyrite, 4 – Fe-dolomite. Svornost shaft, 2nd level, Hildebrand vein. BSE image. Magnification 40×.

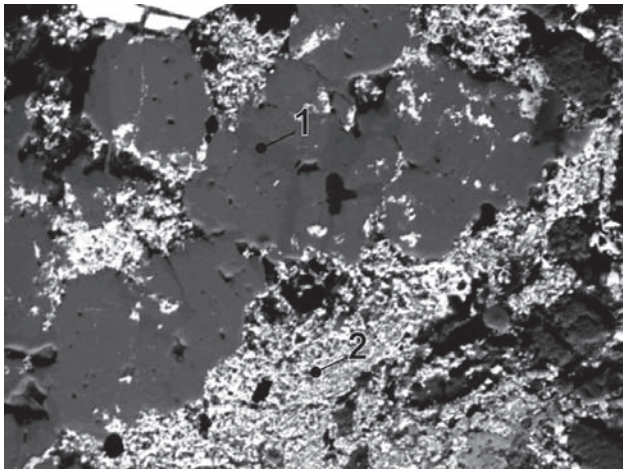

Fig. 28. MP41/D-4. 1 – rammelsbergite, 2 – matildite and mimetite. Svornost shaft, 10th level, Geschieber vein. BSE image. Magnification 600×.

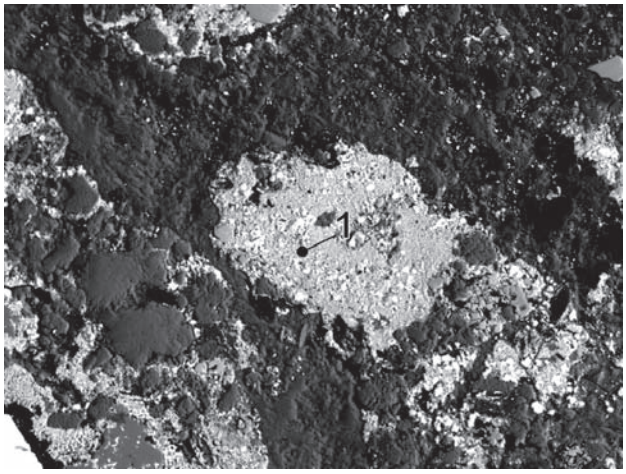

Fig. 29. MP41/D-5. 1 – matildite and Bi-arsenate. Svornost shaft, 10th level, Geschieber vein. BSE image. Magnification 500×.

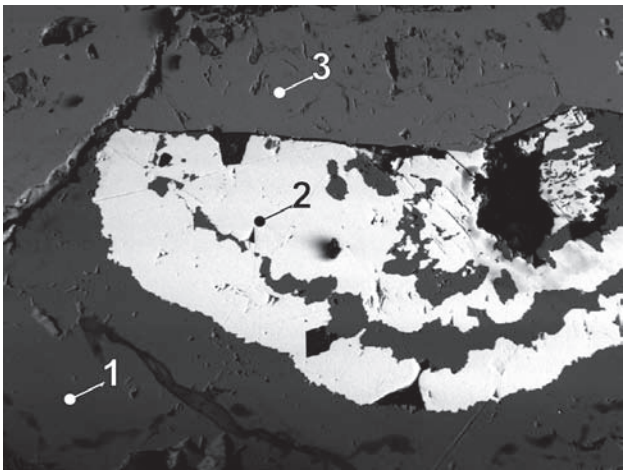

Fig. 30. MP72/A. 1 – sphalerite, 2 – galena, 3 – nickelskutterudite. Eliáš mine, 2A vein. BSE image. Magnification 80×.

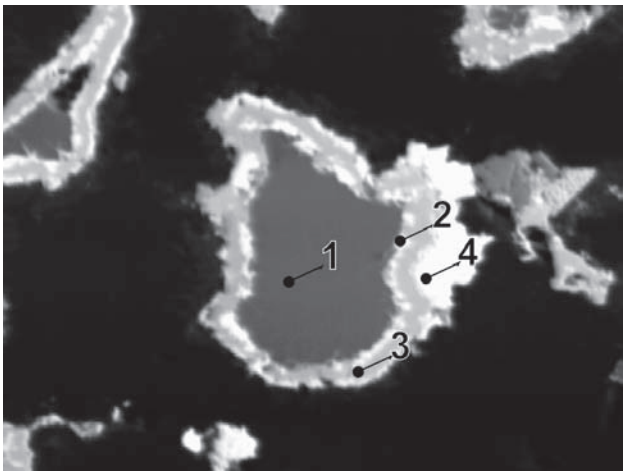

Fig. 31. MP290C/H. 1 – sphalerite, 2 – galena, 3 – wittichenite, 4 – bismuthinite. Barbora shaft, 5th level, vein No. 32. BSE image. Magnification 1600×.

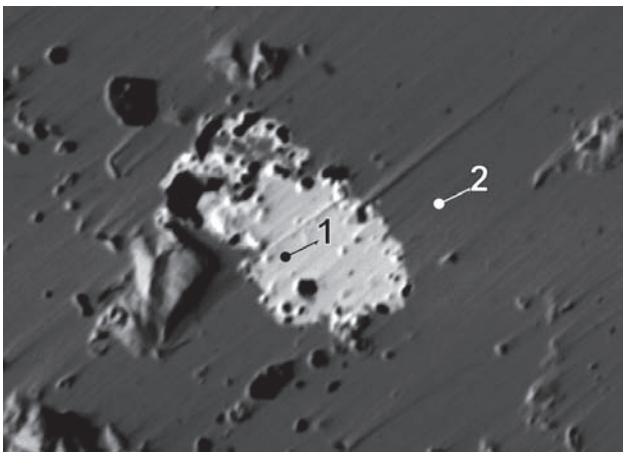

Fig. 32. MP386/1. 1 – wittichenite, 2 – bornite. Plavno, Vladimír mine. BSE image. Magnification 200×.

Post-ore stage

This stage was divided in the literature [351], [423] into several periods, such as *Mn-rich calcite*, *fluorite–barite*, or *opal–quartz*, with variable manifestations in various parts of the deposit. In general, the *post-ore* stage is indistinct in the Jáchymov ore district.

Dominant mineral of this stage is *Mn-rich calcite*, filling offshoots branching from the major NW–SE-striking fault zones. Minerals deposited in this stage show limited effects of younger tectonic deformation. The mineralization of the *fluorite–barite* stage is poorly defined; some *fluorite* occurrences belong to older mineralization stages, and *barite* is too rare. For these reasons, relations of post-ore stage to the general succession of the deposit are not sufficiently clarified.

Gangue minerals of individual mineralization stages

Important gangue minerals include carbonates mostly of the *dolomite – ankerite* series, *quartz* in several generations, minor *fluorite*, and exceptionally *barite* and *siderite*. *Dolomite* and Fe-rich *dolomite* were observed in majority of veins, but pure *calcite* was fairly rare, its separate veinlets formed in later stages of mineralization, partly by the recrystallization of dolomitic carbonates.

Although carbonates represent the main gangue minerals, the total volumes of carbonates are quite low. This situation is responsible for strongly acidic conditions at the deposit. The relatively low carbonate buffering capacity could not neutralize the aggressive arsenate- and sulphate-rich solutions. The solutions circulated through large volumes of the deposit and produced a wide range of secondary minerals.

Quartz of the oldest generation was described as grey, hornstone *quartz*. Drusy *quartz* of the second generation is widespread in the district. It occurs as early deposition in open fractures, later filled by uranium and complex ores. Its deposition marked the beginning of ore mineralization. *Quartz* of the third generation is white, grey and brown, sometimes rather fine-grained. This generation occurs mainly in the parts of veins with carbonates.

Carbonates filled many vein offshoots, especially in sections where the main vein was filled by mylonite. Carbonate formation is represented by *dolomite*, Mg-rich *calcite* or Fe-rich *dolomite* and *ankerite*. Yellow and pink colours prevail but dispersed hematite turns carbonates to brown colour. In the proximity of uranium accumulations the carbonates are typically brick red. *Calcite* crystallized after the deposition of the *dolomite–ankerite* carbonates and occurs only in small amounts. Its typical colour is white. The least common carbonate is *siderite*.

Fluorite is relatively rare. It was deposited on drusy *quartz*, before the crystallization of carbonates, and either before or after the deposition of *uraninite*.

GEOCHEMICAL AND THERMODYNAMIC INTERPRETATION OF HYDROTHERMAL PROCESSES OF INDIVIDUAL MINERALIZATION STAGES

Carbonate–uraninite stage

Modelling of conditions (pH, Eh and concentration) during the formation and remobilization of uraninite

The dissolution or precipitation of solid uranium phases can be modelled using a calculation based on known thermochemical and electrochemical parameters. Unfortunately, natural processes are extremely complicated in the Jáchymov ore district, influenced mainly by the following quantities: U activity, pH, Eh, p, T, activities of O, S, CO_2, HS^-, H_2S, and AsH_3, the ionic strength of solution, type of crystal structure, the size of crystallites, a.o. In order to estimate the values of important variables (pH, Eh, T and U activity), it is necessary to introduce dramatic simplifications and assume limited effects of individual factors.

Chemical analyses of the Jáchymov *uraninite* confirm a composition close to UO_2, with a low component of U^{VI}. General assumptions for a proposed model: reaction in hydrothermal environment in the temperature range of 150–200 °C, moderately oxidizing, neutral or weakly basic conditions; solution contains CO_2, HCO_3^-, Cl^-, SO_4^{2-}, uranium as dominantly U^{VI} carbonate complexes.

On the basis of these assumptions, Eh, pH diagram (Fig. 33) was designed using tabular data [457]. The diagram shows conditions for *uraninite* precipitation, based on the calculation with amorphous UO_2. The graph shows that UO_2 can coexist at a range of pH–Eh conditions with the following ions: $U(OH)_2^{2+}$, $U(OH)_5^-$, UO_2^+. Activities of these ions are also influenced (in equlibrium) under conditions of the above defined environment, with a variable of pH–Eh conditions, by ions: U^{4+}, $U(OH)^{3+}$, UO_2^{2+}, $[UO_2(CO_3)_3]^{4-}$, $[UO_2(CO_3)_2]^{2-}$, UO_2CO_3.

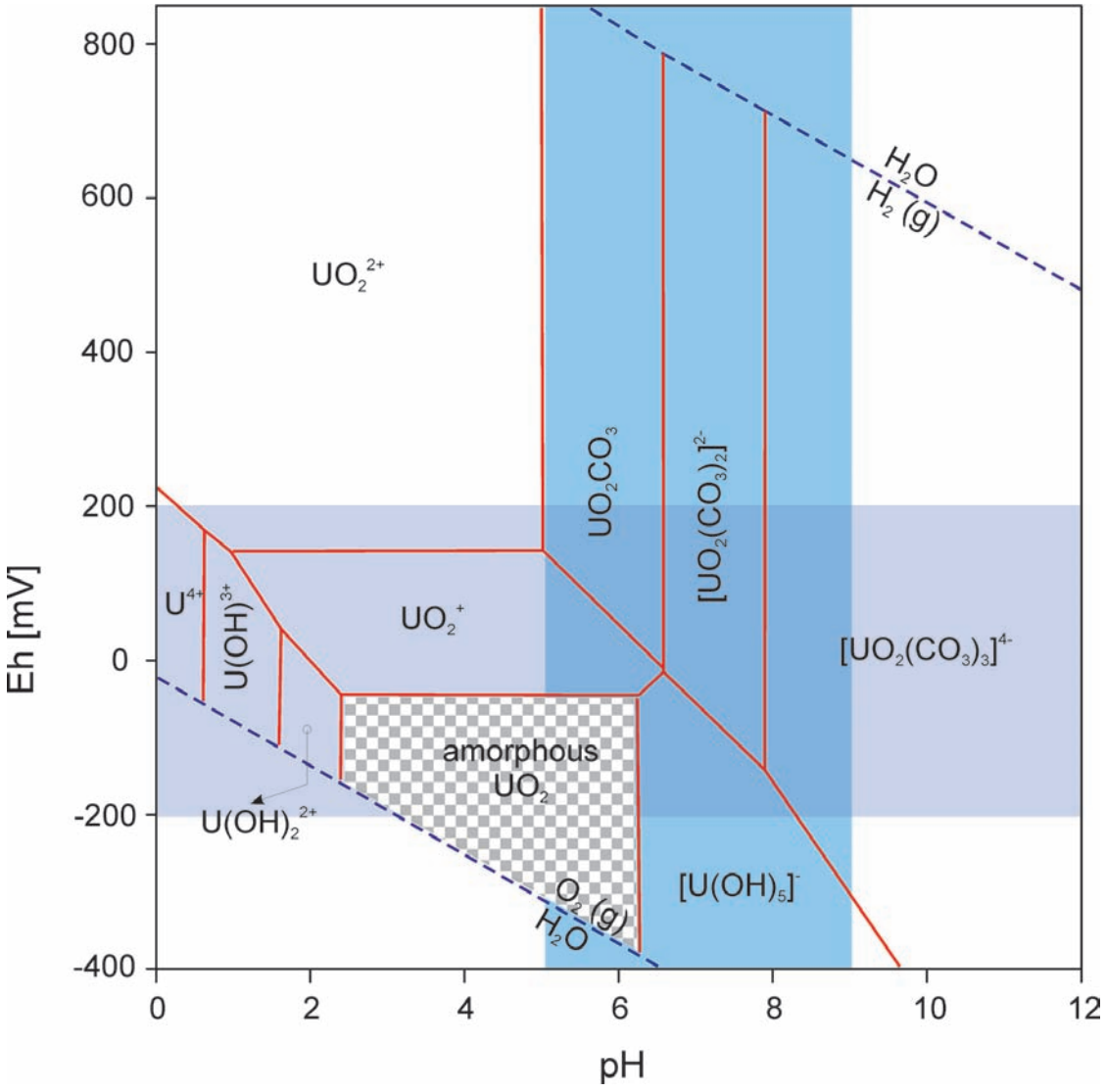

Fig. 33. pH-Eh diagram of equilibria of products of a reaction of uraninite with hydrothermal environment in the system: amorphous uraninite – O_2 – CO_2 – H_2O at 100 °C.

Table 1. Equilibria concentrations in hydrothermal environment in the system: amorphous UO_2–O_2–CO_2–H_2O at 100 °C.

$UO_2 + 2H^+ \leftrightarrow U(OH)_2^{2+}$	
$pH = (-\log [U(OH)_2^{2+}] - 1.32)/2$	$\Delta G°\ (UO_2) = -1031.8$ KJ mol^{-1} $\Delta G°\ (U(OH)_2^{2+}) = -992.4$ KJ mol^{-1}
$UO_2 + 3H_2O \leftrightarrow U(OH)_5^- + H^+$	
$pH = \log [U(OH)_5^-] + 12.2$	$\Delta G°\ (H_2O)_{liq} = -237.1$ KJ mol^{-1} $\Delta G°\ (U(OH)_5^-) = -1641.8$ KJ mol^{-1}
$UO_2 \leftrightarrow UO_2^+ + e^-$	
$E° = 0.325$ V $Eh = E° + 0.059 \log [UO_2^+]$	$\Delta G°\ (UO_2^+) = -968.6$ KJ mol^{-1}
$UO_2^+ \leftrightarrow UO_2^{2+} + e^-$	
$E° = 0.165$ V $Eh = E° + 0.059 \log ([UO_2^{2+}]/[UO_2^+])$	$\Delta G°\ (UO_2^{2+}) = -952.7$ KJ mol^{-1}
$UO_2^{2+} + H_2O + CO_2 \leftrightarrow UO_2CO_3 + 2H^+$	
$\Delta G° = -46.2$ KJ mol^{-1} $pH = (\log ([UO_2CO_3]/[UO_2^{2+}]) - \log p_{CO2} + 8.095)/2$	$\Delta G°\ (CO_2) = -394.4$ KJ mol^{-1} $\Delta G°\ (UO_2CO_3) = -1538.0$ KJ mol^{-1}
$UO_2CO_3 + H_2O + CO_2 \leftrightarrow UO_2(CO_3)_2^{2-} + 2H^+$	
$\Delta G° = -62.7$ KJ mol^{-1} $pH = (\log ([UO_2(CO_3)_2^{2-}]/[UO_2CO_3]) - \log p_{CO2} + 11.25)/2$	$\Delta G°\ (UO_2(CO_3)_2^{2-}) = -2106.8$ KJ mol^{-1}
$UO_2(CO_3)_2^{2-} + H_2O + CO_2 \leftrightarrow UO_2(CO_3)_3^{4-} + 2H^{+-}$	
$\Delta G° = -79.8$ KJ mol^{-1} $pH = (\log ([UO_2(CO_3)_3^{4-}]/[UO_2(CO_3)_2^{2-}]) - \log p_{CO2} + 13.74)/2$	$\Delta G°\ (UO_2(CO_3)_3^{4-}) = -2658.5$ KJ mol^{-1}

$\Delta G°$ – standard free Gibss energy at 25 °C [457],
p_{CO2} – partial pressure of CO_2 (atm)

The overlap area of horizontal and vertical belts in the pH–Eh diagram indicates the most probable range of conditions for the formation of the *carbonate–uraninite* stage of mineralization. A detailed analysis of the overlap area yields the set of equations shown in Table 1.

Based on thermodynamic relations obtained, concentrations of the individual above mentioned ions were calculated under equilibrium conditions such as to correspond to conditions at corners and the centre of the quadrilateral defined in Fig. 33. Inspection of data in Table 2 shows that the role of some ions in the interaction of amorphous UO_2 in hydrothermal environment containing O_2–CO_2–H_2O under variable redox and pH conditions is not significant. This group of ions includes $U(OH)_5^-$, $U(OH)_2^{2+}$, UO_2^+. Some of the reactions are independent of redox conditions, some of variation in pH (see Table 1 with equilibrium reactions).

The review also shows that a combination of a slightly acid environment (pH = 5) with reducing conditions (Eh = –0.2 V) is infavourable for the transport of uranium. Neutral conditions (Eh = 0.0 V, pH = 7) do not represent optimum conditions for U transport either. In acid and oxidizing environment, uranium is mobile in the form of UO_2^{2+} ions, or as undissociated dissolved UO_2CO_3.

Analyses of pH of hydrothermal *quartz* powdered in suspension [351] yielded values in the range of 7.0–8.4. This indicates that hydrothermal environment during the main mineralization stages was probably moderately basic, with pH ~ 8. Based on these assumptions, the combination of Eh = 0.2 V, pH = 5 can be eliminated. A fun-

Table 2. Equilibria reactions, thermochemical and electrochemical interpretation of products in the system: amorphous UO_2–O_2–CO_2–H_2O at 100 °C.

Eh = –0.2 V, pH = 5		**Eh = 0.2 V, pH = 5**		**Eh = –0.2 V, pH = 9**		**Eh = 0.2 V, pH = 9**		**Eh = 0.0 V, pH = 7**	
ion	log (a_i)	ion	log (a_i)	ion	log (a_i)	ion	log (a_i)	ion	log (a_i)
$U(OH)_5^-$	–7.20	UO_2^{2+}	–1.53	$UO_2(CO_3)_3^{4-}$	–1.00	UO_2CO_3	–1.00	$UO_2(CO_3)_2^{2-}$	–3.65
$U(OH)_2^{2+}$	–8.68	UO_2CO_3	–1.62	$UO_2(CO_3)_2^{2-}$	–2.43	$UO_2(CO_3)_2^{2-}$	–1.00	UO_2CO_3	–4.40
UO_2^+	–8.90	UO_2^+	–2.12	$U(OH)_5^-$	–3.20	$UO_2(CO_3)_3^{4-}$	–1.00	$U(OH)_5^-$	–5.20
UO_2^{2+}	–15.08	$UO_2(CO_3)_2^{2-}$	–4.87	UO_2CO_3	–7.18	UO_2^{2+}	–1.53	$UO_2(CO_3)_3^{4-}$	–5.39
UO_2CO_3	–15.18	$U(OH)_5^-$	–7.20	UO_2^+	–8.90	UO_2^+	–2.12	UO_2^+	–5.51
$UO_2(CO_3)_2^{2-}$	–18.43	$U(OH)_2^{2+}$	–8.68	UO_2^{2+}	–15.08	$U(OH)_5^-$	–3.20	UO_2^{2+}	–8.31
$UO_2(CO_3)_3^{4-}$	–24.17	$UO_2(CO_3)_3^{4-}$	–10.61	$U(OH)_2^{2+}$	–16.68	$U(OH)_2^{2+}$	–16.68	$U(OH)_2^{2+}$	–12.68

a_i – calculated equilibria activity of the i-th ion for given pH-Eh conditions and temperature of 100 ºC and pressure of 0.1 MPa.

damental condition for hydrothermal uranium formation is the deposition of U in the form of precipitated and eventually recrystallized gels to phases of a general composition ($U^{4+}_{1-x-y-z}U^{6+}_{x}REE^{3+}_{y}M^{2+}_{z}\square_{v})O_{2+x-0.5y-z-2v}$) [459] through the reduction of mobile ions U^{VI} [458]. Although the existence of U^{VI} is possible in slightly basic reducing environment (on the basis of the above calculations), we suppose, due to the redox potential exchange, that the environment was slightly oxidizing.

Precipitation of UO_2 and conditions of uraninite formation

The above discussed calculations, analyses and assumptions indicate that *uraninite* in the Jáchymov ore district formed from gels, later partly recrystallized, precipitated from slightly basic solutions (pH = 8) carrying ions of $UO_2(CO_3)_3^{4-}$ and $UO_2(CO_3)_2^{2-}$. These ions play the most important role during the transport in hydrothermal environment and in the precipitation of UO_2 gels. The trigger in UO_2 precipitation was a change in pH and Eh caused by the reaction of hydrothermal solutions with materials in the vein or the neighbouring wall-rock, which possibly created sufficient reaction potential and provided for a change in pH; the concentration of $UO_2(CO_3)_3^{4-}$ and $UO_2(CO_3)_2^{2-}$ ions is not directly dependent on Eh. The equations for precipitation of UO_2 can be generally formulated as follows:

$$UO_2(CO_3)_2^{2-} + 2H^+ + 2e^- \leftrightarrow UO_2\downarrow + 2HCO_3^-$$
$$E°(U^{VI}/U^{IV}) \approx 0.2\ V, \text{ estimation from [460]}$$
$$UO_2(CO_3)_3^{4-} + 3H^+ + 2e^- \leftrightarrow UO_2\downarrow + 3HCO_3^-$$

A quantitative course of these reactions depends on the fulfilment of the following conditions:
- reducing condition of sufficient capacity
- change in pH value allowing decomposition of uranyl–carbonate complexes
- environment providing for pressure decrease and release of CO_2
- environment containing sufficient Ca and Mg for the crystallization of carbonates

Reducing conditions in the Jáchymov veins resulted from Fe^{2+}, contained in country rocks, vein carbonates or sulphides; reduction of organic matter played a negligible role owing to its low concentration. The oxidation of sulphides and Fe^{2+} phases allowed a sufficient increase in acidity:

$$2Fe(OH)_2 \leftrightarrow Fe_2O_3\downarrow + H_2O + 2H^+ + 2e^-$$
$$E°(Fe^{III}/Fe^{II}) = -0.86\ V\ [457]$$
$$HS^- \leftrightarrow S°(aq) + 2e^- + H^+$$
$$E°(S°/S^{-I}) = -0.133\ V\ [403]$$
$$2S_2^{2-} \leftrightarrow 4S°(aq) + 4e^-$$
$$E°(S°/S^{-I}) = -0.30\ V\ [461]$$
$$S^{2-} \leftrightarrow S°(aq) + 2e^-$$
$$E°(S°/S^{-II}) = -0.48\ V\ [403]$$

In the second step, oxidation continued with the participation of H_2O:

$$S°(aq) + 3H_2O \leftrightarrow SO_2(OH)^- + 5H^+ + 4e^-$$
$$E°(S^{IV}/S°) = -0.66\ V\ [403]$$
$$S^{IV}O_2(OH)^- + H_2O \leftrightarrow SO_4^{2-} + 3H^+ + 2e^-$$
$$E°(S^{VI}/S^{IV}) = -0.94\ V\ [403]$$

And finally, a shift in the redox equation $U^{VI} \Rightarrow U^{IV}$, caused by the consumption of HCO_3^- ions via precipitation of Ca^{2+} and Mg^{2+}, in favour of the final products – *calcite* and *dolomite*:

$$2HCO_3^- + 2Ca^{2+} \leftrightarrow 2CaCO_3 + H_2O$$

$$4HCO_3^- + 2Mg^{2+} + 2Ca^{2+} \leftrightarrow 2CaMg(CO_3)_2 + H_2O.$$

It is probable that the redox mechanisms discussed will vary and oscillate, which may result in local reversal of reactions toward the initial components. Thus with the onset of the *arsenic–sulphide* stage, with an increase in redox potential and acidity, mechanisms started to operate, facilitating transition of U in solution via oxidation $U^{IV} \Rightarrow U^{VI}$:

$$UO_2\downarrow + 2H_2O \leftrightarrow U_3O_8\downarrow + 4H^+ + 4e^-$$
$$E°(U^{5.3}/U^{IV}) = 0.278\ V\ \text{(crystalline)}\ [460]$$
$$E°(U^{5.3}/U^{IV}) = 0.031\ V\ \text{(amorphous)}\ [460]$$
$$U_3O_8\downarrow + H_2O + H^+ \leftrightarrow 3\ UO_2(OH)^+ + 2e^-$$
$$E°(U^{VI}/U^{5.3}) = 0.707\ V\ [460]$$
$$UO_2\downarrow \leftrightarrow UO_2^{2+} + 2e^-$$
$$E°(U^{VI}/U^{IV}) = 0.221\ V\ [460]$$

The ions UO_2^{2+} and $UO_2(OH)^+$ are very mobile, which resulted in frequent rejuvenation (remobilization) of the original *uraninite*.

The wall-rock alteration affected mainly Mg and Fe minerals, Ca was probably transported by mineralizing solutions. The oxidized forms of Fe were deposited mainly in the abundant *hematite* pigment in vein fillings as well as in altered wall-rock.

Precipitation of Fe oxides

Carbonate crystals near *uraninite* contain thin layers rich in Fe oxides, indicating growth zones. Formation of such growth zones can be explained by the mechanism of redox reactions. Due to the oscillation in Ca^{2+}/Fe^{2+} ratio and varying Eh and pH, the successive growth zones contain a variable Fe^{II} component. During the episode with lower pH and increased oxidizing capacity of the solution, U in *uraninite* was dissolved at the formation of mobile UO_2^{2+}:

$$UO_2\downarrow \leftrightarrow UO_2^{2+} + 2e^-$$

Over a short distance, UO_2^{2+} ions were reduced back to UO_2 through reaction with Fe^{2+}, bound in a thin layer of ankeritic carbonate:

$$UO_2^{2+} + 2FeCO_3 \leftrightarrow 2Fe^{3+} + 2CO_3^{2-} + UO_2\downarrow$$

The released Fe^{3+} ions were precipitated in a neutral or slightly basic environment, buffered by carbonates, following the reaction:

$$2Fe^{3+} + 6(OH)^- \leftrightarrow 3H_2O + Fe_2O_3\downarrow$$

$$Fe^{3+} + 3(OH)^- \leftrightarrow H_2O + FeO(OH)\downarrow$$

In contrast to the precipitated and relatively stable Fe_2O_3, the newly precipitated UO_2 was easily soluble and re-mobilized over longer distances.

Redox potential of hydrothermal environment after the carbonate–uraninite stage

The following model is proposed for the interpretation and prediction of the deposition of ore components in hydrothermal veins (*arsenide* and *arsenic–sulphide* stages) based on a change of redox conditions controlling mineral crystallization.

Estimates of Gibbs free energy were calculated for the oxidation of the anionic part of minerals as a basis for estimates of reducing capacity or stability/instability under changing redox properties of the environment in dependence of Eh on hydrothermal solutions. The following equation was employed:

$$AN^\circ + ne^- \leftrightarrow AN^{n-},$$

where AN represents anionic part of an arsenide, sulpharsenide or sulphide molecule.

In a formal way, Gibbs free energy is assigned to mean the value of valence of atoms in anionic part of each molecule (*n*), based on the relation between the exchange of free energy and electromotoric strength (EMS) given by the relation:

$$\Delta G_A^\circ = -n\ F\ E^\circ,$$

where F is Faraday constant and E° is standard reduction potential of the equations below. The following reactions hold for a neutral or slightly basic environment:

$2S^\circ + 2e^- \leftrightarrow (S_2)^{2-}$ $E^\circ(S^\circ/S^{-I}) = -0.25$ V [403]

$2As^\circ + 2e^- \leftrightarrow (As_2)^{2-}$ $E^\circ(As^\circ/As^{-I}) \approx -0.50$ V (estimated value from [403])

$3As + 2e^- \leftrightarrow (As_3)^{2-}$ $E^\circ(As^\circ/As^{-2/3}) \approx -0.33$ V (estimated value from [403])

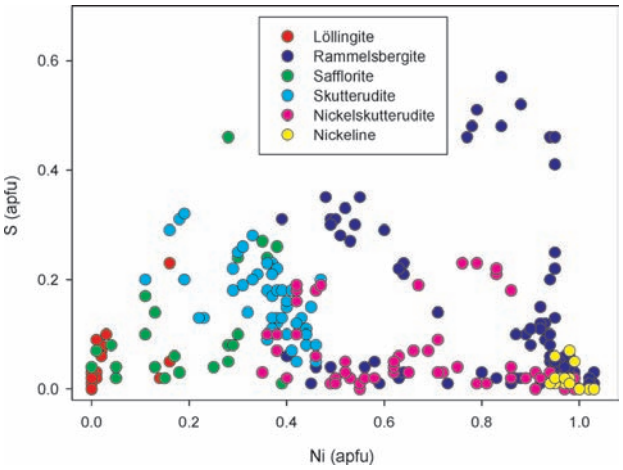

Fig. 34. Sulphur vs. nickel content in selected arsenides of the arsenide mineralization stage.

Table 3. Oxidation state and modified Gibbs free energies (ΔG°) for selected arsenides, sulpharsenides and sulphides of Ni, Co, Fe.

	As				S				Me					results	
mineral	**OS**	**n**	**E°**	**ΔG°**	**OS**	**n**	**E°**	**ΔG°**	**Me**	**n_K**	**OS**	**Me**	**OS**	**$\Sigma\Delta G^\circ_{AN}$**	**$\Sigma\Delta G^\circ_{AN}/n_K$**
nickeline	–3.0	1	–1.37	132				0	Ni	1	3.0			132	**132**
löllingite	–1.0	2	–0.50	97				0	Fe	1	2.0			97	**97**
clinosafflorite	–1.0	2	–0.50	97				0	Co	1	2.0			97	**97**
safflorite	–1.0	2	–0.50	97				0	Co	1	2.0			97	**97**
rammelsbergite	–1.0	2	–0.50	97				0	Ni	1	2.0			97	**97**
skutterudite	–0.7	3	–0.33	96				0	Co	1	2.0			96	**96**
nickel-skutterudite	–0.7	3	–0.33	96				0	Ni	1	2.0			96	**96**
arsenopyrite	–1.0	1	–0.50	48	–1.0	1	–0.25	24	Fe	1	2.0			72	**72**
alloklas	–1.0	1	–0.50	48	–1.0	1	–0.25	24	Co	1	2.0			72	**72**
gersdorffite	–1.0	1	–0.50	48	–1.0	1	–0.25	24	Ni	1	2.0			72	**72**
pyrrhotite				0	–2.0	8	–0.48	371	Fe	7	2.3			371	**53**
marcazite				0	–1.0	2	–0.25	48	Fe	1	2.0			48	**48**
pyrite				0	–1.0	2	–0.25	48	Fe	1	2.0			48	**48**
sternbergite				0	–2.0	3	–0.48	139	Fe	3	2.5	Ag	1.0	139	**46**
sphalerite				0	–2.0	1	–0.48	46	Zn	1	2.0			46	**46**
chalcopyrite				0	–2.0	2	–0.48	93	Cu	2	2.0	Fe	2.0	93	**46**
acanthite				0	–2.0	1	–0.48	46	Ag	2	1.0			46	**23**
proustite	3.0	1	0.68	–66	2.0	3	–0.25	72	Ag	3	1.0			7	**2**
arsenic	0.0	1		0				0	As	1				0	**0**

grade of oxidation

OS – oxidation states ([592], [593], [594]),
n, (n_k) – anion (or cation) atoms per formula unit,
E° (V) – estimated standard reduction potential,
ÄG° (kJ/mol) – free Gibbs energy (calculated from estimated standard reduction potentials).

The $\Delta G_A°$ values express the ability of atoms to accept electrons and increase their oxidation state. Minerals with a higher $\Delta G_A°$ value would precipitate more readily in reducing conditions, and minerals with a lower value or corresponding to zero would preferentially crystallize in environment with a higher oxidation potential.

Mean values of valence (oxidation state) of all atoms in anionic part of the arsenides molecule are generally lower than in sulpharsenides and sulphides (see Table 3).

Application of the above calculations to the interpretation of crystallization succession of the *five-element* assemblage in the Jáchymov ore district shows (Table 3) that the oxidation potential of the *arsenide* stage was very low, probably the lowest among all the mineralization stages. An important role during the *arsenide* stage was played by the pH of the environment.

Also important is the role of sulphur [447], which did not take part in mineral crystallization due to its low fugacity (or high fugacity of As) at the beginning of the *arsenide* stage. Later, when S fugacity increased, sulphur partially participated in the mineralization process. Interesting are significant sulphur contents (Fig. 34) in the arsenides (*rammelsbergite, skutterudite*) of the *arsenide* stage. On the other hand, some sulpharsenides are deficient in S, due to the high As fugacity. This is seen in *gersdorffite* with As/S ratio varying from the normal value 1 : 1 to extreme values of 1.85 : 0.15. Minerals of such composition still retain *gersdorffite* structure and isotropic optical behaviour (see figures for *gersdorffite*).

Arsenide stage

Crystallization of silver and bismuth dendrites

Ag and Bi are delivered in the form of Cl complexes, mainly $AgCl_2^-$ and $BiCl_4^-$. The absence of Ag_2S in the primary *silver* accumulations indicates a deficiency in HS^- ions, which would preferentially precipitate sulphides [see below $\beta(AgHS) » \beta(AgCl_2^-)$], in comparison with the chlorides. Besides this, free HS^- ions in coexistence with $AgCl_2^-$ complexes spontaneously oxidize to SO_4^{2-} ions:

$$HS^- + 4H_2O + 8AgCl_2^- \leftrightarrow SO_4^{2-} + 8Ag + 16Cl^- + 9H^+$$

Hydrothermal solutions were strongly saline (ca. 20 % $CaCl_2$, NaCl), weakly acid (pH ~ 6–7), and S fugacity was probably low.

Mercury shows similar chemical properties of chloride complexes as those characteristic of Ag, resulting in joint precipitation of the two metals. This is indicated by the occurrence of mercurian *silver* with up to 2 wt. % Hg in rims of the old *silver* dendrites.

Estimate of concentration of mobile Ag or Bi ions:

Silver: For the reaction

$$Ag^+ + 2\,Cl^- \leftrightarrow AgCl_2^-$$

it is at 20 °C $\log(\beta_2) = 5.14$ [463], $\log(K_s(AgCl)) = -9.75$ [463]

This gives equilibrium concentration $[AgCl_2^-] = \beta_2 K_s [Cl^-] = 2.45 \cdot 10^{-5} [Cl^-]$ mol/l. The concentration of dissolved $AgCl_2^-$ ions in the presence of 20 % and 0.1 % NaCl at 20 °C is $8.6 \cdot 10^{-5}$ mol/l and $4.9 \cdot 10^{-7}$ mol/l, respectively, of free Ag.

In case of a parallel existence of two hydrothermal solutions with comparable contents of HS^- a Cl^- ions at a given time, the HS^- ion will be preferentially instrumental in Ag transport. For the reaction

$$Ag^+ + 2HS^- \leftrightarrow Ag(HS)_2^-$$

is $\log(\beta_2) = 17.43$ [463], and for *argentite (acanthite)* dissociation:

$$Ag_2S \leftrightarrow 2Ag^+ + S^{2-}$$

is $K_S = -48.8$ [463]. From this follows that $[Ag(HS)_2^-] = \beta_2[Ag^+][HS^-]$, where $[Ag^+] = \sqrt[3]{2K_s}$. For $[HS^-]$ concentration of, e.g., 0.001 mol/l, $[Ag(HS)_2^-] = 0.014$ mol/l.

Bismuth: For the reaction

$$Bi^{3+} + 4Cl^- \leftrightarrow BiCl_4^-$$

at 20 °C, $\log(\beta_4) = 5.52$ is obtained [463]. This shows that Bi in chloride solution will behave in a similar way as Ag. Nevertheless, stability of the complex $BiCl_4^-$ is strongly influenced by Cl^- concentration and the value of pH:

$BiCl_4^- + H_2O \leftrightarrow BiOCl(s) + 2H^+ + 3Cl^-$, where $\log K = -1.20$ [463].

Growth of native Ag and Bi dendrites

As noted above, spontaneous precipitation of native Ag or Bi in the form of dendrites proceeded by the reduction of Ag or Bi chloro-complexes:

$$AgCl_2^- + e^- \leftrightarrow Ag + 2Cl^-$$

$$BiCl_4^- + 3e^- \leftrightarrow Bi + 4Cl^-$$

The rapid growth of skeletal crystals was caused by increased concentration of [Ag] ~10^{-5} mol/l (a similar situation applies to Bi), and the existence of reducing environment. The latter was represented in this mineralization stage mainly by *biotite*-bearing rocks with increased Fe^{II} and by rocks with finely dispersed *pyrite*.

The released Fe^{2+} in neutral or slightly basic environment is readily oxidized to Fe_2O_3. In an oxidation environment, the oxidation of *pyrite* readily takes place following the equation:

$$FeS_2 + 8H_2O \leftrightarrow Fe^{2+} + 2SO_4^{2-} + 16H^+ + 14e^-.$$

Dendritic *silver* and *bismuth* crystals precipitated rapidly at separated sites. The following factors are considered important for their separated precipitation:

– difference in standard electrochemical potential $E°(Bi^{3+}/Bi) = 0.320$ V, $E°(Ag^{+}/Ag) = 0.799$ V.
– differences in the stability of $AgCl_2^-$ and $BiCl_4^-$ complexes in hydrothermal environment. The anion $BiCl_4^-$ readily changes to BiOCl with a low solubility.

Precipitation of Ni–Co–Fe polyarsenides

Precipitation of polyarsenides took place under increasingly reducing conditions imposed by high arsine (AsH_3) contents. Arsine is dissolved in brine fluids; dissociation to ions AsH_2^- ($\log(K) \approx -155$ [425]) is negligible.

Batches of fluids containing Ni, Co, Fe were closely tied to AsH_3, at fairly low S fugacity, in a neutral or weakly acid environment. Under these conditions Ni, Co, Fe aqua chloro-complexes formed, facilitating the transport of these elements. Complexes with ligand AsH_3 were probably also formed: $[Ni(H_2O)_u(AsH_3)_vX_w]^{2-w}$, where u+v+w = 4 or 6, X = OH, Cl; co-ordination of the central atoms (Ni,Co,Fe) of the above group of complexes is 4 or 6, with co-ordination 6 being the most common.

The disintegration of these complexes, caused mainly by a change in pressure and temperature, resulted in the precipitation of arsenides (polyarsenides in general). The appearance, chemical composition and physical properties of some arsenide aggregates suggest a rapid precipitation, which indicates high concentrations of the complexes.

The formation of arsenides–diarsenides–triarsenides is closely related to the redox potential of the environment. Based on the redox model (see *Redox potential of hydrothermal environment after carbonate-uraninite stage* above), it is possible to say that the redox potential values play a leading role in the precipitation, and control the type of arsenide to be precipitated. Our observations of several generations of individual arsenides indicate repeated changes in redox environment. Local variation in available oxidants, such as UO_2^{2+}, Fe^{3+}, O a.o., may have caused these changes.

Arsine oxidation in acid environment can proceed easily through the reaction with wall-rocks (Fe^{3+}, Mn^{3+}) and with components brought by the mineralizing solutions (UO_2^{2+}, O a.o.). Small interposed layers of *uraninite* separating some arsenide layers serve as evidence of the participation of UO_2^{2+} ions in the deposition of polyarsenides.

The chemical analyses of arsenides (in particular triarsenides) reveal a variable composition (Ni, Co, Fe) of successive growth zones. Hydrothermal solutions of the first stage show the highest contents of metal in the order of Ni > Co ≥ Fe, and, at the same time, the lowest values of Eh potential, thus providing for the crystallization of *nickeline*, with the highest content of metals and with the lowest valency state of As:

$$[Ni(H_2O)_u(AsH_3)_vX_w]^{2-w} \leftrightarrow NiAs + 3H^+ + wCl^- + uH_2O + (w-1)AsH_3 + e^-$$

or in a simplified form (mild oxidation):

$$Ni^{2+} + AsH_3 \leftrightarrow Ni^{III}As^{-III} + 3H^+ + e^-$$

The deposition of diarsenides and triarsenides proceeded in a similar manner only in the environment with an increased Eh potential. The following equations express multistage redox processes:

$$Ni^{2+} + AsH_3 + H_2S \leftrightarrow Ni^{II}As^{-I}S^{-I} + 5H^+ + 3e^-$$

$$Ni^{2+} + 2AsH_3 \leftrightarrow Ni^{II}As_2^{I} + 6H^+ + 4e^-$$

$$Ni^{2+} + 3AsH_3 \leftrightarrow Ni^{II}As_3^{-II/III} + 9H^+ + 7e^-$$

Oxidation states of As and Ni are adopted from [592], [593], and [594].

Variation in As fugacity and other parameters in the course of the *arsenide* stage is shown in Fig. 1. Increasing acidity, not significantly buffered by carbonates, is characteristic of these processes. The increased acidity of solutions resulted in the alteration of wall-rocks and breccias, characterized by the formation of clay minerals (see figure for *kaolinite* in the encyclopaedic section).

In a general way, the experimentally confirmed trend in the precipitation of arsenides corresponds to a gradually increasing oxidation potential of the whole fracture system, following the succession:

arsenides ⇒ diarsenides ⇒ triarsenides,

Oscillations in the redox potential resulted in a partial repetition of this succession. The above equations of arsenide precipitation indicate increasing acidity in the process.

Antimony was probably transported in the form of stibine (SbH_3), in a similar way as arsenic in the form of AsH_3. In the final stage of polyarsenide precipitation, the fugacity of Sb increased due to the supply of additional Sb.

Dissolution of Ag and Bi dendrites

Dendritic crystals of Ag and Bi were quantitatively overgrown by Ni, Co, Fe polyarsenides and some other minerals. After the deposition of polyarsenides, the dendritic aggregates of native Ag and Bi were nearly quantitatively dissolved.

It appears that the dissolution of Ag and Bi was not accomplished purely by chemical dissolution (metals were surrounded by polyarsenides), but rather through electrochemical dissolution. Metallic Ag or Bi enclosed in non-conducting polyarsenides behaved as an electro-

chemical half-cell in solutions with a high content of Cl^- ions. The potential of such half-cell is:

$$Ag(s) + Cl^- \leftrightarrow AgCl(s) + e^- \qquad E°_1(Ag^+/Ag) = 0.222\ V.$$

Released AgCl in such environment is dissolved:

$$AgCl(s) + Cl^- \leftrightarrow AgCl_2^-(aq)$$

To achieve electrolysis resulting in the dissolution of Ag, the second part of the electrochemical cell must represent a redox half-cell with a potential higher than 0.222 V. With regard to ions available in the hydrothermal environment at Jáchymov, the following reaction is considered:

$$Fe^{3+} + e^- \leftrightarrow Fe^{2+} \qquad E°_2(Fe^{3+}/\ Fe^{2+}) = 0.771\ V$$

$$O_2 + 4H^+ + 4e^- \leftrightarrow 2H_2O \qquad E°_2(O/\ O^{2-}) = 1.229\ V$$

This redox reaction applies only to a slightly acid environment. The oxidation ability of UO_2^{2+} is insufficient for the dissolution of Ag: $E°(U^{VI}/U^{IV}) = 0.221$ V.

The resulting electrochemical cell:

$$Ag(s) + Cl^- + Fe^{3+} \leftrightarrow AgCl(s) + Fe^{2+}$$

will generate under standard conditions potential of $\Delta E° = E°_2 - E°_1 = 0.549$ V (see Fig. 35). Assuming that the cell will operate under connection of the "electrodes" by salt solution, Ag will be dissolved and $\Delta G°$ value will be negative: $\Delta G° = -nF\Delta E° = -52.9$ kJ/mol. To obtain activity relation $[Fe^{3+}]/[Fe^{2+}]$, let's assume that $\Delta G = 0 = \Delta G° + RT \ln(K)$, resulting in $\Delta G° = -RT \ln(K) = -RT \ln([Fe^{2+}]/[Fe^{3+}])$. For the reaction to proceed ($\Delta G° < 0$), it is necessary to have $[Fe^{2+}]/[Fe^{3+}] = \exp(-\Delta G°/RT) = 3.5 \cdot 10^5$. This condition will be satisfied under hydrothermal conditions in a certain range of pH values. Hydrolysis of Fe^{3+} ions is proceeding following the reaction:

$$Fe^{3+} + H_2O \leftrightarrow Fe(OH)^{2+} + H^+$$
$$\log(K_1) = -2.20,\ \log(K_s) = -36.5\ [463];$$

this implies that approximately $[Fe^{3+}] = ([H^+]cFe)/K$, where cFe is the total content of dissolved Fe. For example, for pH = 6, $cFe = 10^{-2}$ mol/l will be $[Fe^{3+}] = 1.6 \cdot 10^{-5}$ mol/l.

In the course of Ag dendrite dissolution, Ag is mobilized and deposited in other parts of the ore veins. It becomes bound mainly in sulphides and sulpharsenides, only to a limited degree it is precipitated as native Ag. In the transport of Ag from dissolved dendrites, HS^- ions played probably a much more important role in the formation of stable complexes AgHS and $Ag(HS)_2^-$, where $\log(\beta_1) = 13.48$ and $\log(\beta_2) = 17.43$ [589]

$$Ag + HS^- \leftrightarrow AgHS$$

$$Ag + 2HS^- \leftrightarrow Ag(HS)_2^-$$

Increased acidity results in the precipitation of Ag_2S (*argentite*):

$$2Ag(HS)_2^- + 2H^+ \leftrightarrow Ag_2S + 3H_2S.$$

Precipitation of Ag_2S is also triggered by an increased redox potential:

$$4H_2O + Ag(HS)_2^- \leftrightarrow Ag_2S + SO_4^{2-} + 10H^+ + 8e^-.$$

Precipitation of silver sulphosalts (*proustite*, *xanthoconite*) proceeds through the reaction of Ag with complex ions $H_2As_3S_6^-$ or $H_2AsS_3^-$ [590]:

$$9AgHS + H^+ + H_2As_3S_6^- \leftrightarrow 3Ag_3AsS_3 + 6H_2S$$

These reactions take place owing to increasing S fugacity, redox potential and acidity of the hydrothermal environment.

Dissolution of Bi was accomplished by similar electrochemical processes as in the case of Ag.

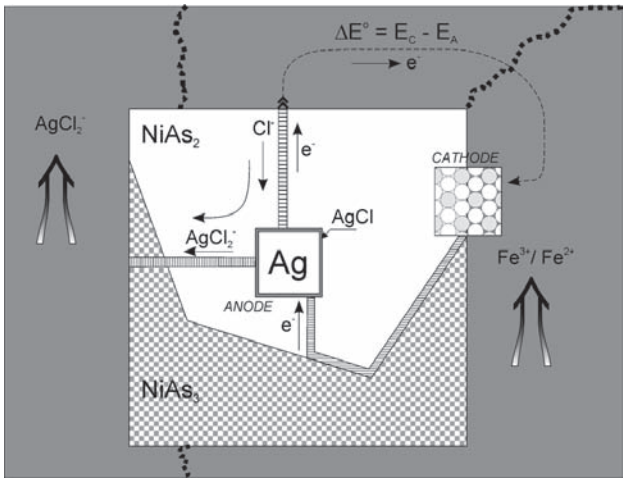

Fig. 35. Schematic image of electrodissolution of native silver.

Arsenic–sulphide stage

Precipitation of arsenic

Arsine-rich solutions, after removal of metallic ions (Ni, Co, Fe), quantitatively precipitated native As under moderately acid conditions (pH ~ 6) in an oxidizing environment. Sulphur fugacity was insufficient for the production of As–S phases. *Realgar* was observed only as insignificant accumulations in the association with *arsenic*.

The following relation applies in an acid environment:

$$AsH_3 \leftrightarrow As^\circ + 3H^+ + 3e^-$$
$$E^\circ_1(As^\circ/As^{-III}) = -0.225 \text{ V [403].}$$

The reaction can take place spontaneously, if under standard conditions ΔG° of the whole reaction is negative, i.e. $\Delta E^\circ > 0$. If $\Delta E^\circ = E_2^\circ - E_1^\circ$, where E_2° represents redox reaction, where $E^\circ_2 > E^\circ_1$, i.e., for $E^\circ_2 > -0.225$ V, oxidation of arsine to As will take place. In other words, arsine oxidation in acid environment will proceed easily [591], in particular with Fe^{3+}, UO_2^{2+}, O_2 and other oxidants characterized by a positive standard redox potential.

Precipitation of base metal sulphides and sulpharsenides

Arsenic fugacity abruptly decreased during this period but S fugacity was gradually increasing. Redox poten-

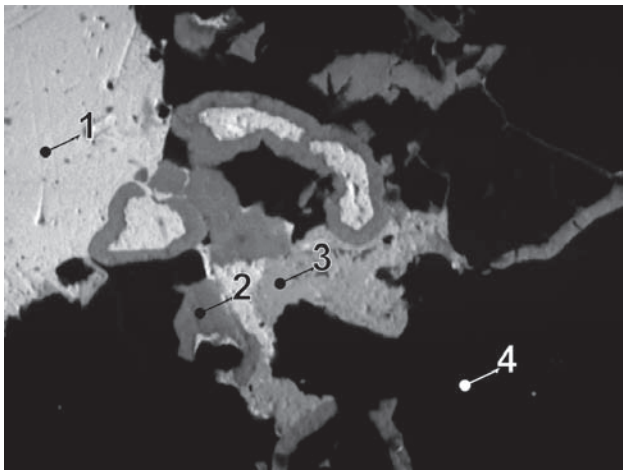

Fig. 38. J167P/1. 1 – bismuth, 2 – Bi–S–Mo, 3 – bismutite, 4 – quartz. Eliáš mine, 180 m level, 2A vein. BSE image. Magnification 540x.

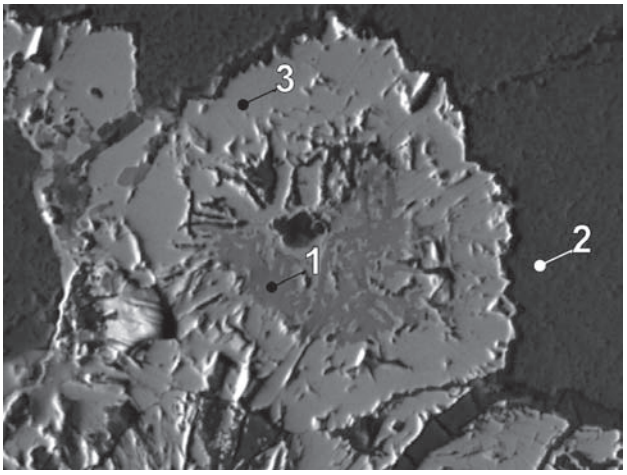

Fig. 36. J116P/D-1. 1 – Ag–Fe-sulphides containing (Ni, As), 2 – pyrite, 3 – nickel–skutterudite. Svornost shaft, 8th level, Geschieber vein. BSE image. Magnification 540×.

Fig. 39. J167P/4. 1 – bismuth, 2 – Bi–S–Mo, 3 – bismutite, 4 – quartz. Eliáš mine, 180 m level, 2A vein. BSE image. Magnification 270×.

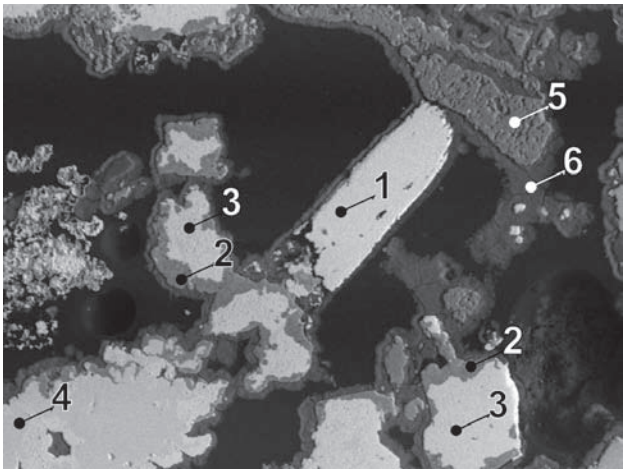

Fig. 37. J141P/D. 1 – bismuth, 2 – Ag-millerite, 3 – argentite, 4 – proustite, 5 – pyrite, 6 – annabergite. Eliáš mine. BSE image. Magnification 130×.

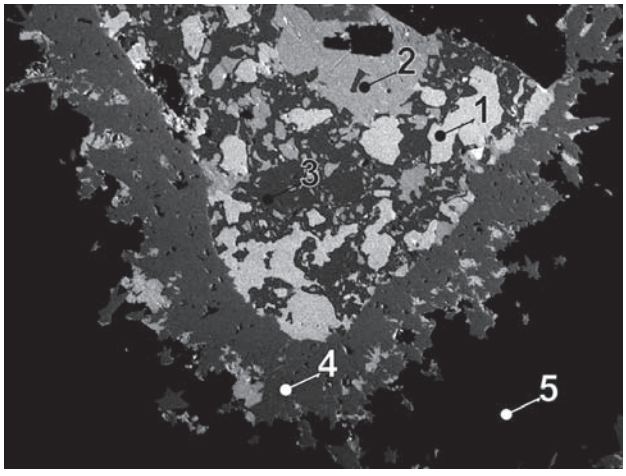

Fig. 40. J171P/D. 1 – silver, 2 – argentite, 3 – argentopyrite, 4 – löllingite, 5 – dolomite. Zimní Eliáš mine. BSE image. Magnification 160×.

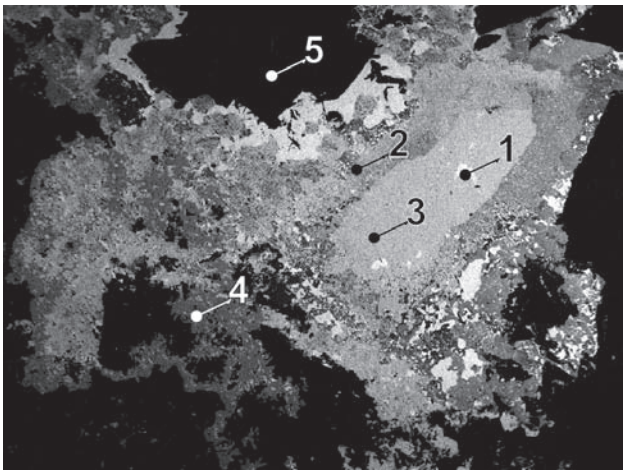

Fig. 41. J171P/F. 1 – silver, 2 – silver, argentopyrite and pyrargyrite, 3 – pyrargyrite, 4 – löllingite, 5 – dolomite. Zimní Eliáš mine. BSE image. Magnification 27×.

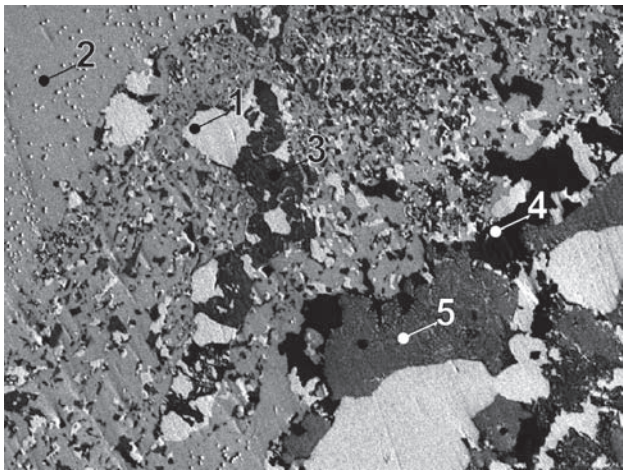

Fig. 42. J171P/F-1. 1 – silver, 2 – pyrargyrite, 3 – argentopyrite, 4 – chalcopyrite, 5 – argentopyrite decomposed into acanthite and pyrite. Zimní Eliáš mine, dump. BSE image. Magnification 320×.

tial and acidity were increased in fractures of the vein system.

Minerals containing metallic elements (Cu, Ag, Pb, Zn, Fe) crystallized. The first generation precipitated from chloride or hydrosulphide complexes of hydrothermal solutions. Crystallization was triggered by temperature decrease, for example:

$PbCl_3^- + H_2S \leftrightarrow PbS + 3Cl^- + 2H^+$

$ZnCl_4^{2-} + H_2S \leftrightarrow ZnS + 4Cl^- + 2H^+$

$2AgHS \leftrightarrow Ag_2S + H_2S$

precipitation was positively influenced by increasing acidity, for example:

$2Ag(HS)_2^- + 2H^+ \leftrightarrow Ag_2S + 3H_2S$

$9Me^{I}HS + H^+ + H_2As_3S_6^- \leftrightarrow 3Me^{I}_3AsS_3 + 6H_2S$

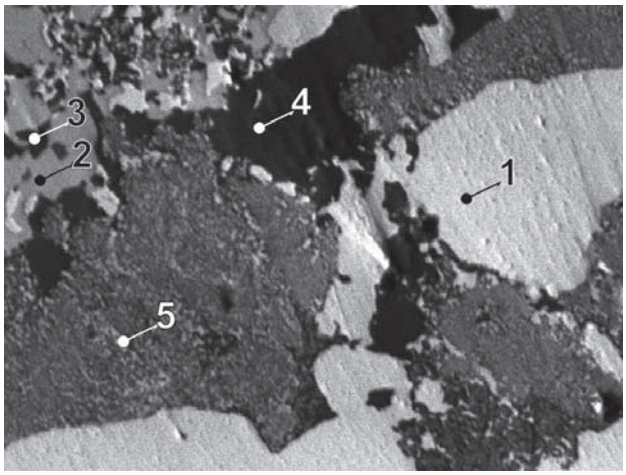

Fig. 43. J171P/F-2. 1 – silver, 2 – pyragyrite, 3 – argentopyrite, 4 – chalcopyrite, 5 – argentopyrite decomposed into acanthite and pyrite. Zimní Eliáš mine. BSE image. Magnification 720×.

Redox potential of the arsenic–sulphide mineralization stage: oxidation states of arsenic, sulpharsenides and Ag, Cu sulphides

The majority of elements in minerals of this paragenesis have a higher oxidation state compared to the *arsenide* stage. A significant participation of sulphur, and to a lesser extent antimony, is observed in this mineralization stage.

The oxidation state of As changed from –III or –I to 0 and in part to +III,

Table 4. Values of sulphur fugacity [log f_{S2} (atm.)] of selected minerals of Jáchymov district, calculated for temperatures of 60–200 °C.

sample	60	80	100	120	140	160	180	200
vaesite	–22.5	–20.7	–19.0	–17.5	–16.2	–15.0	–13.9	–12.8
realgar	–22.7	–20.9	–19.3	–17.8	–16.5	–15.3	–14.2	–13.2
xanthoconite/argentite	–22.9	–21.2	–19.7	–18.3	–17.1	–16.0	–14.9	–14.0
proustite/argentite	–23.6	–21.8	–20.1	–18.7	–17.4	–16.2	–15.1	–14.1
argentite	–24.0	–22.4	–21.0	–19.8	–18.7	–17.6	–16.7	–15.8
acanthit	–24.6	–22.9	–21.4	–20.1	–18.9	–17.8	–16.8	–15.9
bismuthinite	–26.3	–24.3	–22.6	–21.1	–19.7	–18.4	–17.2	–16.2
stibnite	–27.4	–25.2	–23.3	–21.6	–20.0	–18.6	–17.3	–16.1
matildite	–27.2	–25.2	–23.5	–21.9	–20.5	–19.2	–18.0	–16.9
covellite	–28.1	–26.1	–24.3	–22.7	–21.3	–20.0	–18.8	–17.7
argentopyrite	–26.5	–24.9	–23.6	–22.4	–21.2	–20.2	–19.3	–18.5
pyrite/pyrrhotite	–31.3	–28.7	–26.3	–24.2	–22.3	–20.6	–19.0	–17.6
pyrite	–36.5	–33.8	–31.5	–29.3	–27.4	–25.7	–24.1	–22.6
chalcocite	–38.5	–36.0	–33.8	–31.9	–30.1	–28.5	–27.1	–25.7
chalcopyrite	–41.5	–38.7	–36.2	–34.0	–31.9	–30.1	–28.4	–26.9
galena	–41.5	–38.8	–36.3	–34.0	–32.0	–30.2	–28.5	–27.0
pyrrhotite	–41.9	–39.2	–36.7	–34.5	–32.5	–30.7	–29.0	–27.5
molybdenite	–43.9	–40.8	–38.0	–35.4	–33.2	–31.1	–29.2	–27.5
sphalerite	–70.3	–65.7	–61.6	–58.0	–54.7	–51.7	–49.0	–46.5

Data were calculated from ΔG^o values published in [449].

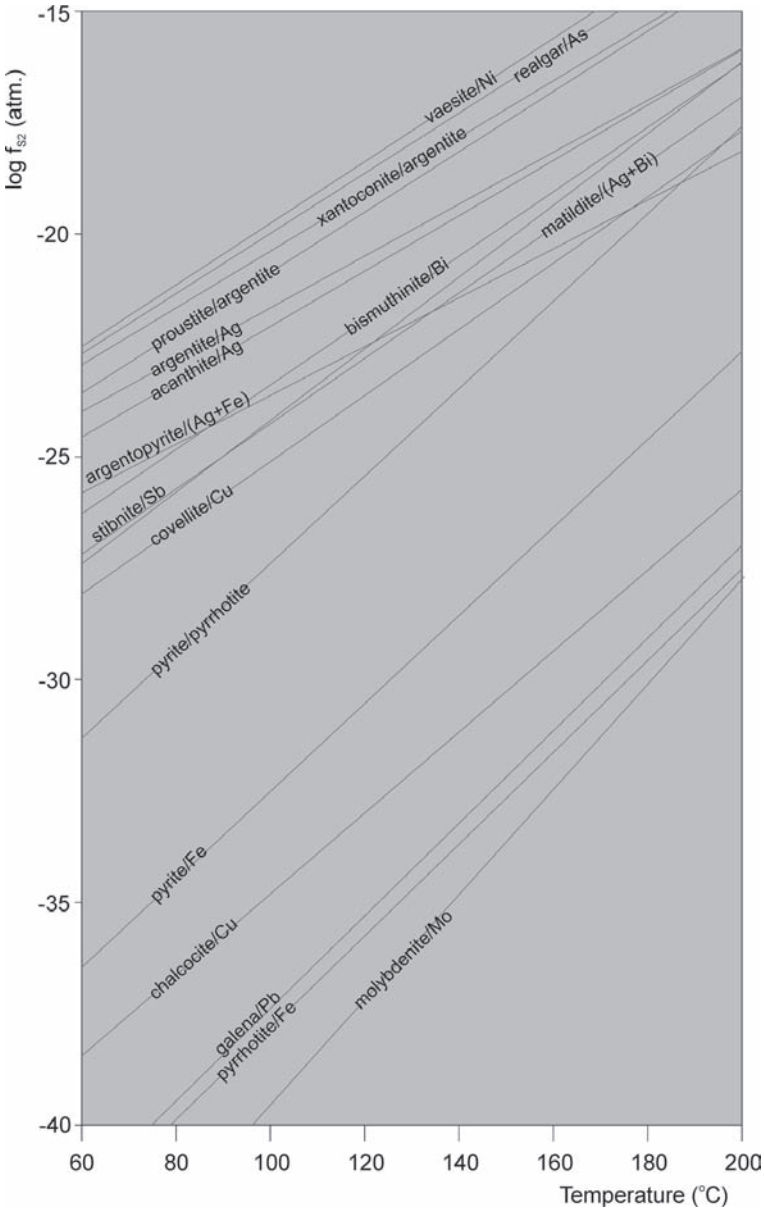

Fig. 44. Sulphur fugacity (log f_{S2}) vs. temperature for selected minerals of the Jáchymov district.

resulting in accumulations of native *arsenic*, Ag, Cu sulphosalts with the anion $[As^{III}S_3]^{3-}$ or of *realgar*. At the end of the *arsenic–sulphide* stage, the activity of AsH_3 significantly decreased (see Fig. 1, 36–43).

Hydrothermal solution supplied some Sb jointly with dominant As, resulting in the crystallization of Ag, Pb, and Cu sulphosalts with the anions $[Sb^{III}S_3]^{3-}$, $[Sb^{III}S_2]^-$, $[Sb_4S_{13}]^{14}$, $[SbS_4^{5-}]$, a.o. The fairly increased Sb content in the Hildebrand vein is responsible for the formation of Sb paragenesis: *antimony*, *stibnite*, *arsenic*, *dyscrasite*, *miargyrite*, *pyrargyrite*, *robinsonite*, *stibarsen*, and intermetallic phases AsSb and BiSb.

Manifestations of increased oxidation potential are seen also in the deposition of silver. The main part of silver is bound as Ag^+ cation in the above named sulphosalts, or as *acanthite*, *argentopyrite* or *sternbergite*.

Oxidizing environment is also indicated by *hematite* pigmentation in dolomitic carbonate, which is the main gangue mineral of the *arsenic–sulphide* stage.

Role of sulphur in the hydrothermal process

Nearly all stages of mineralization include some sulphides, mainly *pyrite* and *sphalerite*. This shows that sulphur fugacities in the hydrothermal solutions were slightly above zero.

It is assumed that sulphur was transported in solutions as HS^-, H_2S or in anionic complexes with metallic elements $[Me^{I}(HS)_n]^{n-1}$ or $[Me^{II}(HS)_n]^{n-2}$. Relations between these components were influenced by many factors, including p–T, pH, Eh, contents of metallic elements, oxygen, etc., and regulated the dissolution or precipitation of sulphides, sulpharsenides and sulphosalts. A major factor triggering crystallization of these species was sulphur fugacity (f_{S2}). Table 4 presents S fugacities for common sulphur-bearing minerals of all mineralization stages. The relations are documented in Fig. 44. The reference temperature of 160 °C represents average temperature of all mineralization stages. The succession of minerals from bottom to top (Table 4) generally corresponds to the formation of S-minerals in the Jáchymov ore district. The first minerals to crystallize were *sphalerite*, *pyrrhotite* and *galena*, the late minerals include sulphosalts and Bi-, Ag-sulphides.

GRAPHIC INTERPRETATION OF CHEMICAL ANALYSES – SUBSTITUTION TRENDS

This chapter gives interpretation of chemical analyses (for source data see *Primary minerals* – encyclopaedic part) of the most common ore minerals of the Jáchymov district.

Attention is focused mainly on minerals of the *arsenide* mineralization stage. Repeated variations in the composition and Eh potential of the mineralizing solutions during the deposition of minerals of this stage resulted in the crystallization of minerals with highly variable composition. Ni/Co/Fe and S/As ratios show isomorphous substitutions in mineral structures [490]. Owing to the high fugacities of As, minerals with extremely high contents of As crystallized. This concerns mainly *pyrite* containing nearly 11 wt. % As and *gersdorffite* containing over 62 mol. % As. In spite of these chemical differences, the minerals retain their crystal structure and optical properties (isotropic behaviour).

Group of diarsenides and triarsenides of Ni–Co–Fe

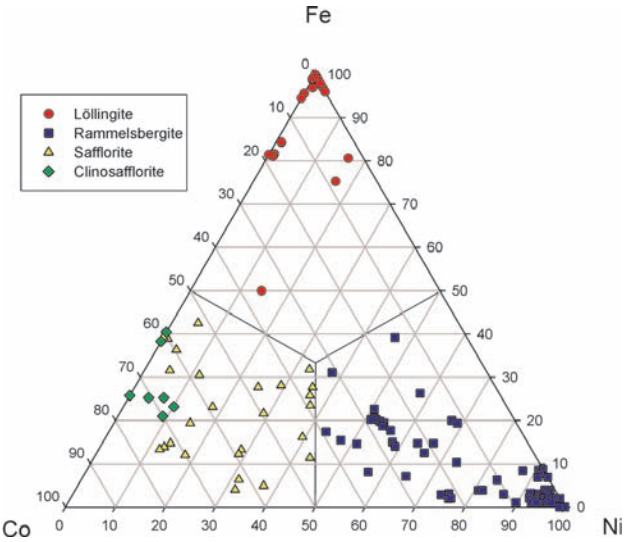

Fig. 45. Ni–Co–Fe ratio (atomic values) in selected diarsenides of the arsenide mineralization stage.

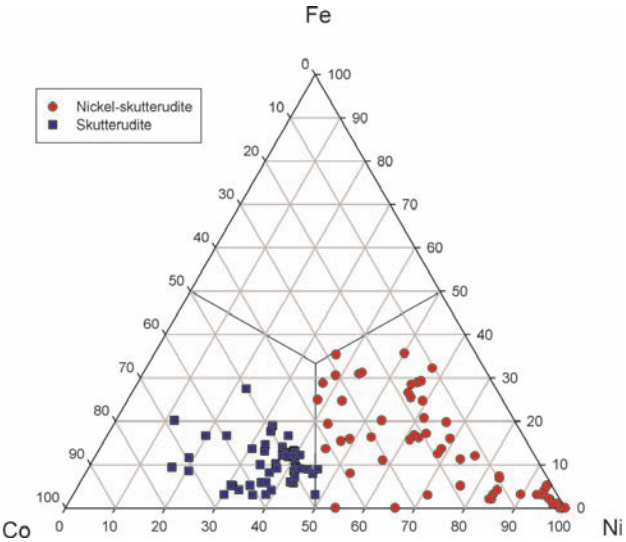

Fig. 46. Ni–Co–Fe ratio (atomic values) in selected triarsenides of the arsenide mineralization stage.

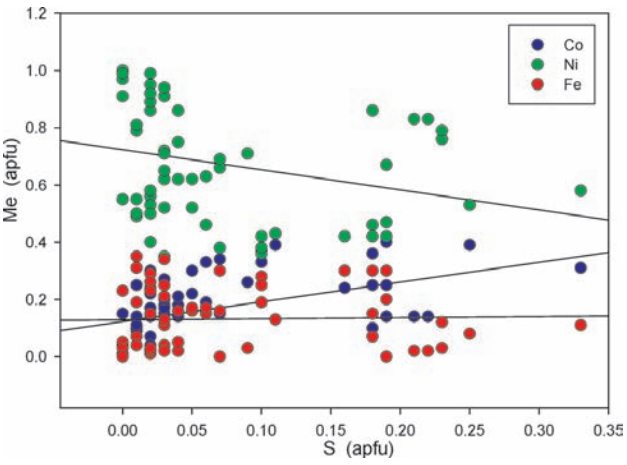

Fig. 47. Me (Me=Ni,Co,Fe) (apfu) vs. S (apfu) for nickel-skutterudite. Regression lines express correlation trends of analytical data.

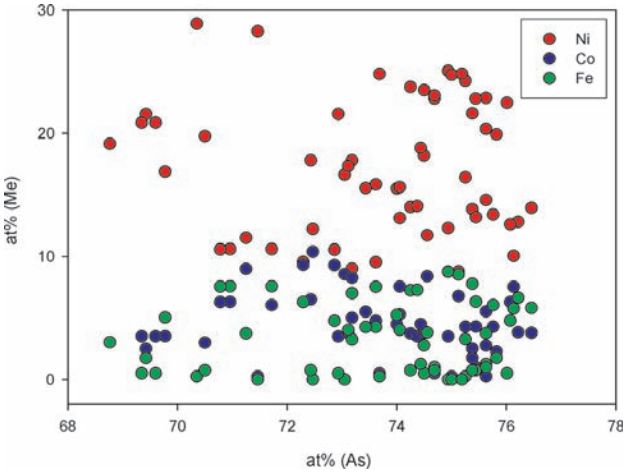

Fig. 48. Me (Me=Ni,Co,Fe) (apfu) vs. As (apfu) for nickel-skutterudite.

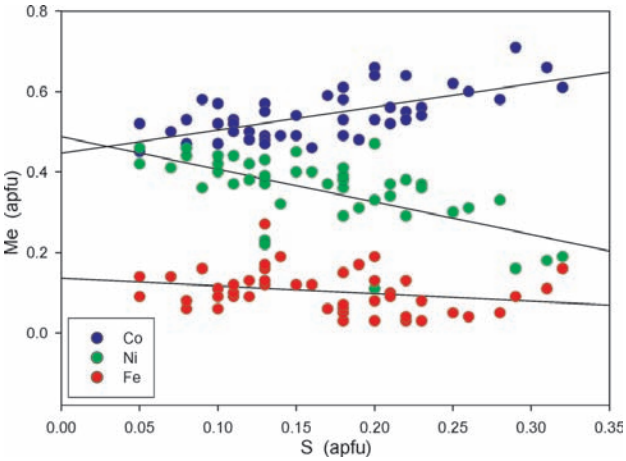

Fig. 49. Me (Me=Ni,Co,Fe) (apfu) vs. S (apfu) for skutterudite.

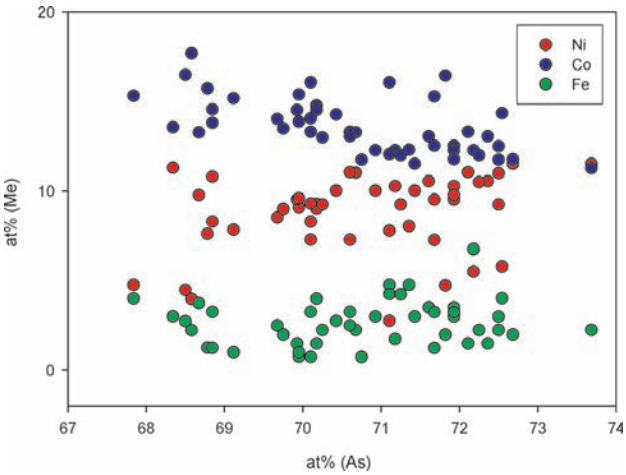

Fig. 50. Me (Me=Ni,Co,Fe) (apfu) vs. As (apfu) for skutterudite.

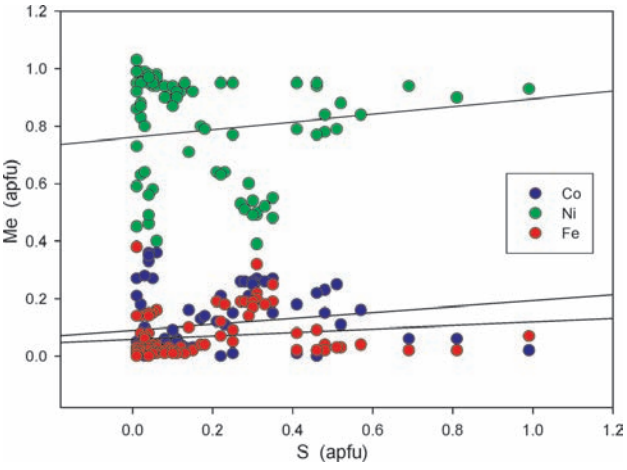

Fig. 51. Me (Me=Ni,Co,Fe) (apfu) vs. S (apfu) for rammelsbergite. Regression lines express correlation trends of analytical data.

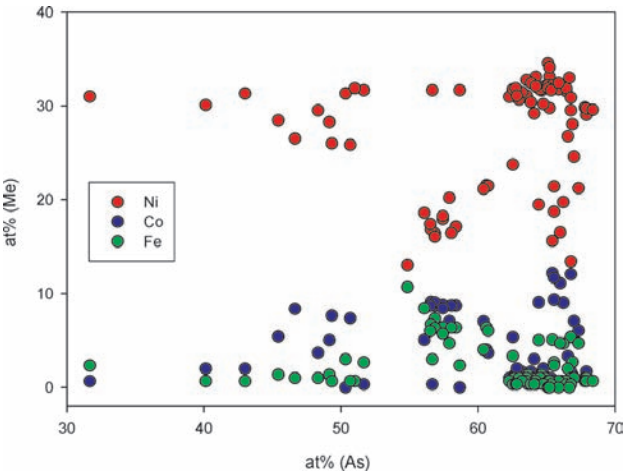

Fig. 52. Me (Me=Ni,Co,Fe) (at.%) vs. As (at.%) for rammelsbergite.

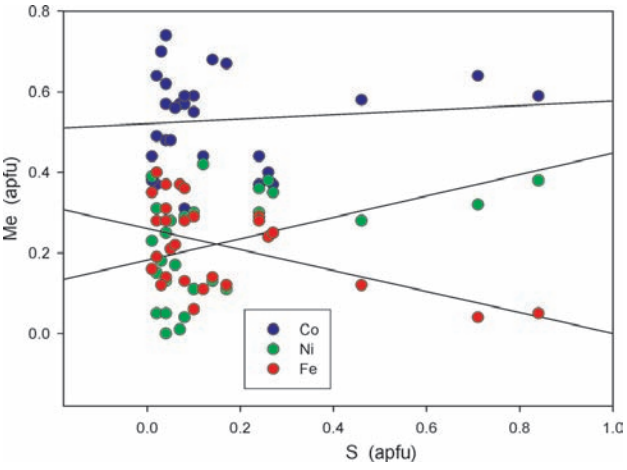

Fig. 53. Me (Me=Ni,Co,Fe) (apfu) vs. S (apfu) in safflorite. Regression lines express correlation trends of analytical data.

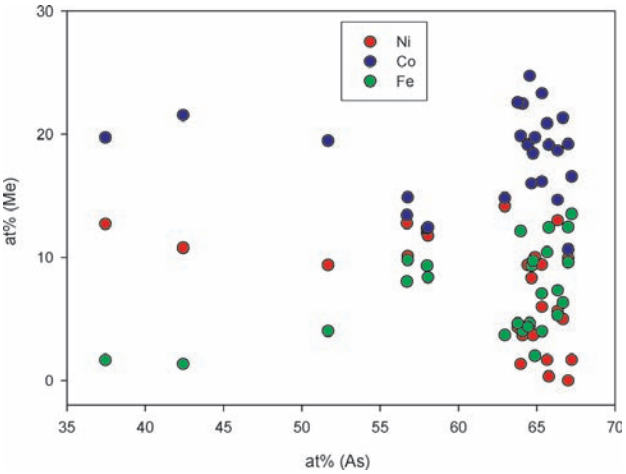

Fig. 54. Me (Me=Ni,Co,Fe) (at.%) vs. As (at.%) for safflorite.

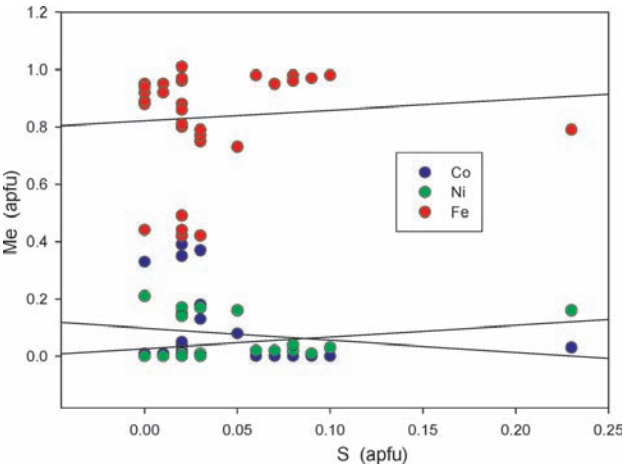

Fig. 55. Me (Me=Ni,Co,Fe) (apfu) vs. S (apfu) for löllingite. Regression lines express correlation trends of analytical data.

Correlation of chemical composition and structural parameters of diarsenides

From the mineralogical point of view, crystal shapes of *Ni-löllingite* (sample J171P) and *Fe-safflorite* (Fig. 57) similar to six-pointed stars are very interesting. The crystals are triplets with twinning on plane (101) [348]. This type of twinning is limited by the condition $a/c = \tan(60)$, where a, c are unit-cell parameters. This condition is shown in Fig. 56 by a grey band. The a/c ratio is a function of chemical composition – substitution of Ni, Co, Fe, so that the condition for the formation of a hexagram (Fig. 58) is met only for particular compositions, with *löllingite* containing substantial Ni or *safflorite* containing Fe. These conditions are often met in Jáchymov (see Ni–Co–Fe ternary diagrams for *safflorite* and *löllingite* – Fig. 45). Triplets do not occur with *rammelsbergite*, since its a/c ratio (near 1.33) is

far from the value of tan(60). Triangular symbols in the diagram below, plotting outside the grey belt, correspond to relatively pure *löllingite* without triplets.

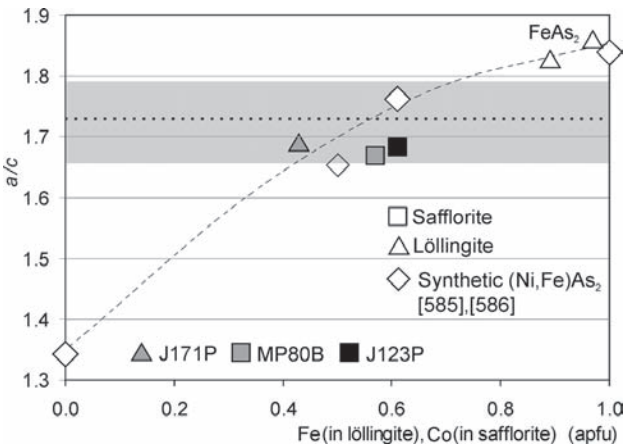

Fig. 56. *a/c* ratio of unit-cell parameters vs. Ni (in löllingite) and Fe (safflorite) (apfu). Grey belt shows range of a/c values compatible with formation of six-pointed star triplets.

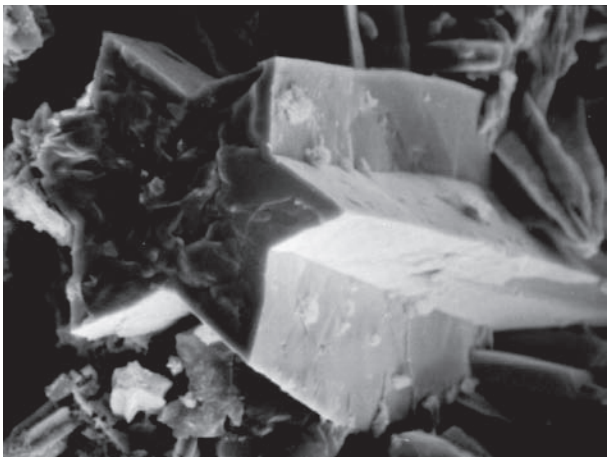

Fig. 57. J171P. Ni-löllingite triplets on (101) plane in the shape of six-pointed star. Zimní Eliáš mine. SE image. Magnification 1450×. Photo A. Gabašová.

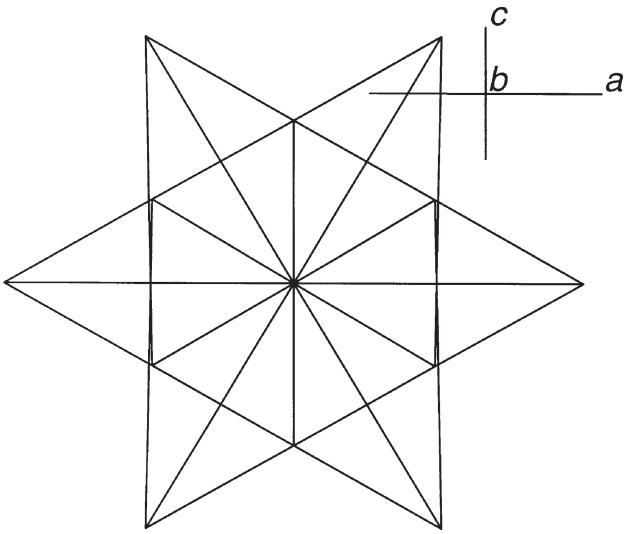

Fig. 58. Computer model of löllingite triplet with twinning plane (101), in projection on *ac* plane. Unit-cell parameter ratio *a/c* = 1.732.

Variation of Ni, Co, Fe against As in selected polyarsenides and sulpharsenides

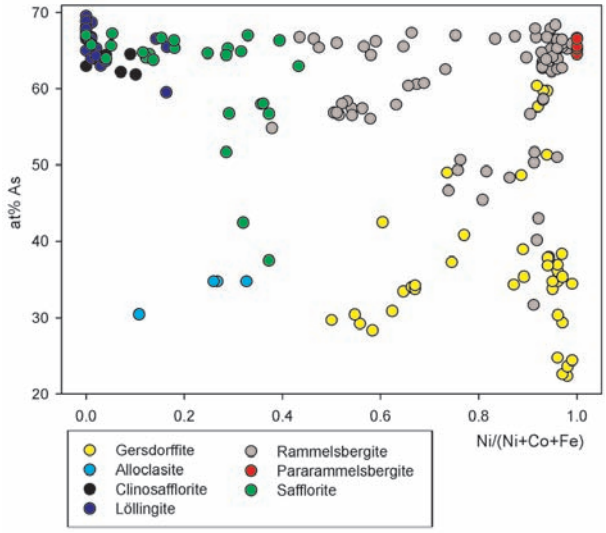

Fig. 59. As (at%) vs. atomic ratio Ni/(Ni+Co+Fe) for selected minerals of the arsenide mineralization stage.

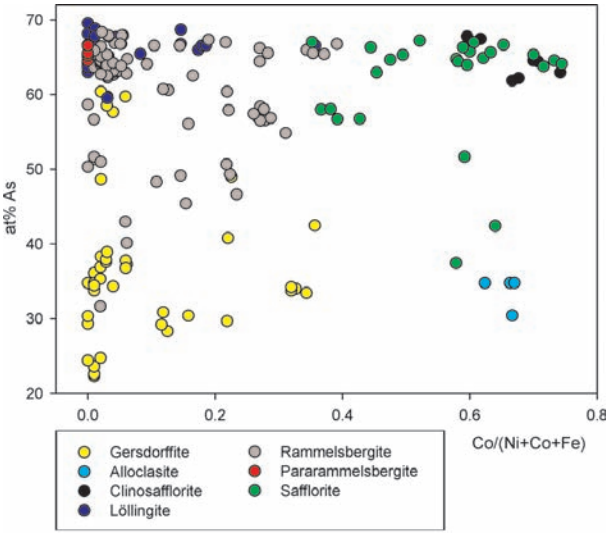

Fig. 60. As (at%) vs. atomic ratio Co/(Ni+Co+Fe) for selected minerals of the arsenide mineralization stage.

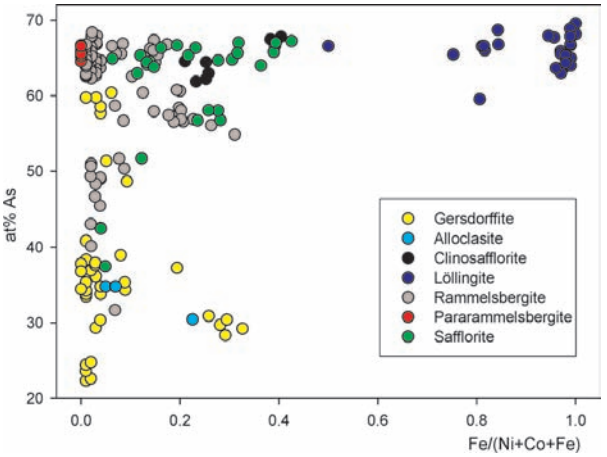

Fig. 61. As (at%) vs. atomic ratio Fe/(Ni+Co+Fe) for selected minerals of the arsenide mineralization stage.

Group of sulpharsenides *(gersdorffite, arsenopyrite, alloclasite)*

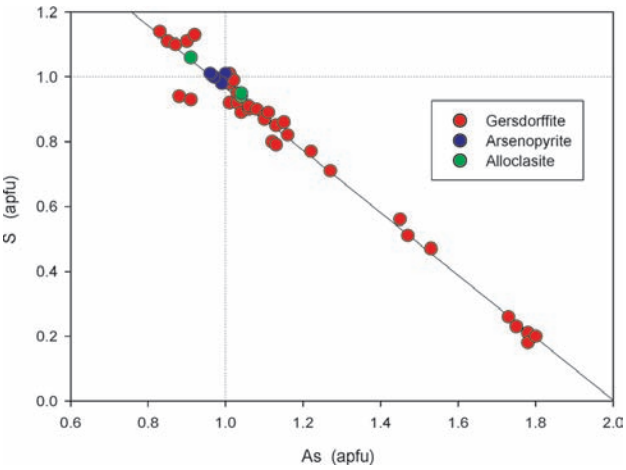

Fig. 62. S vs. As (apfu) in selected sulpharsenides of the arsenide mineralization stage.

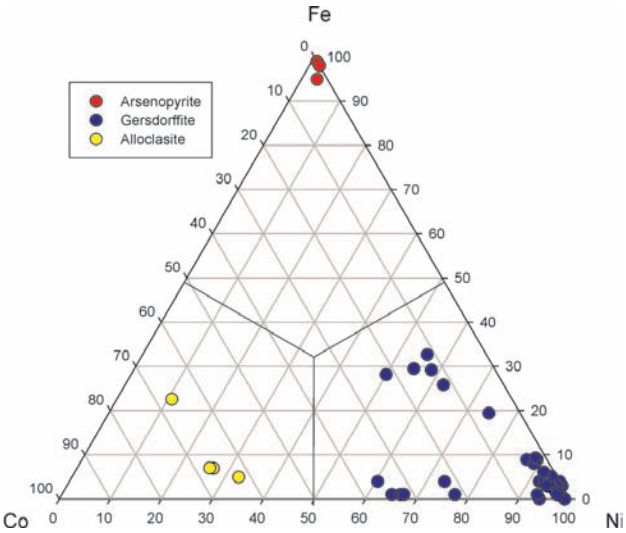

Fig. 63. Ni–Co–Fe ratio (atomic values) in selected sulpharsenides of the arsenide mineralization stage.

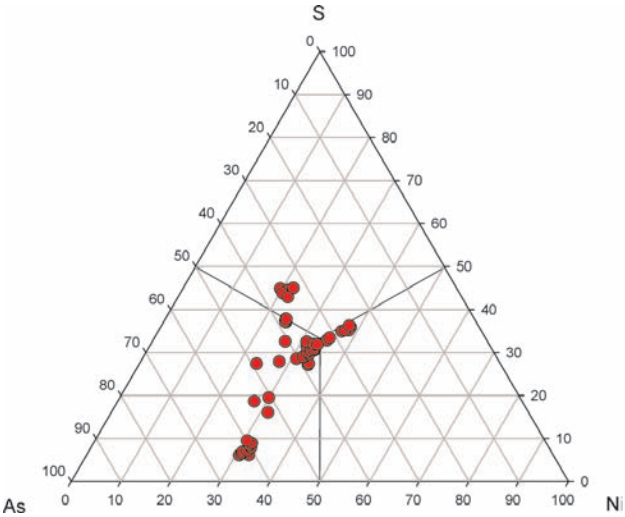

Fig. 64. S–As–Ni ratio (atomic values) in gersdorffite.

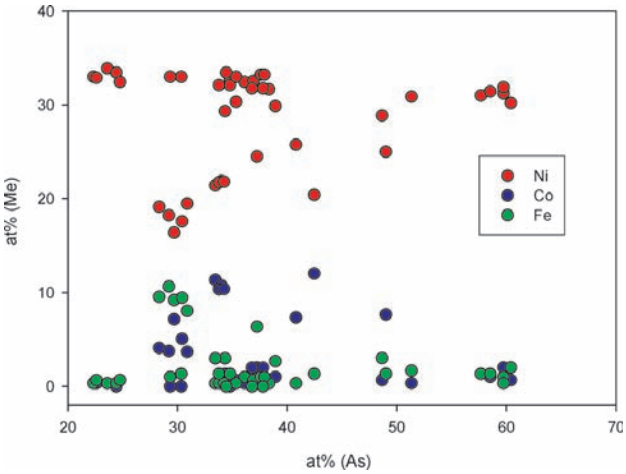

Fig. 65. Me (Me=Ni,Co,Fe) (at.%) vs. As (at.%) for gersdorffite.

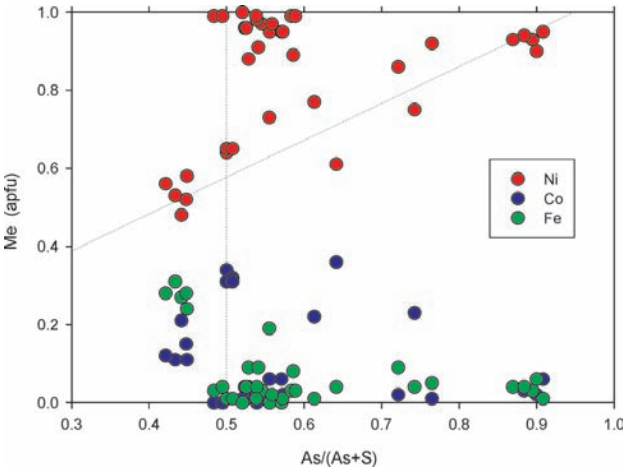

Fig. 66. Gersdorffite. Me (Me=Ni,Co,Fe) (apfu) is correlated with atomic ratio As/(As+S)

Group of disulphides (*pyrite, marcasite, vaesite*)

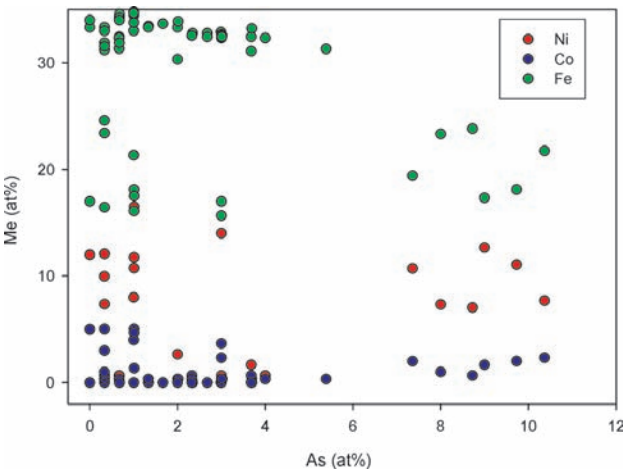

Fig. 67. Me (Ni,Co,Fe) (at.%) vs. As (at.%) for pyrite.

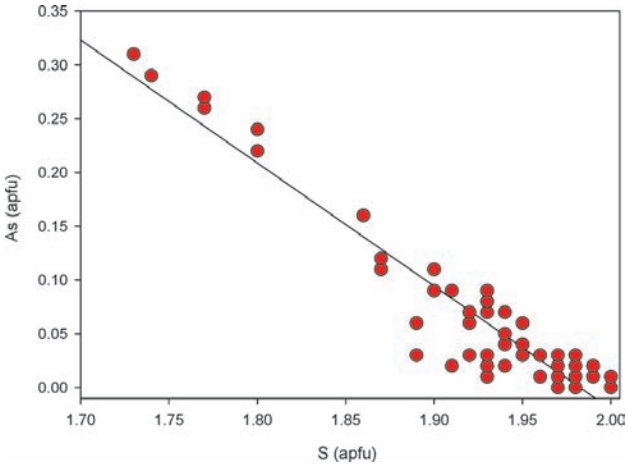

Fig. 68. As (apfu) vs. S (apfu) for pyrite.

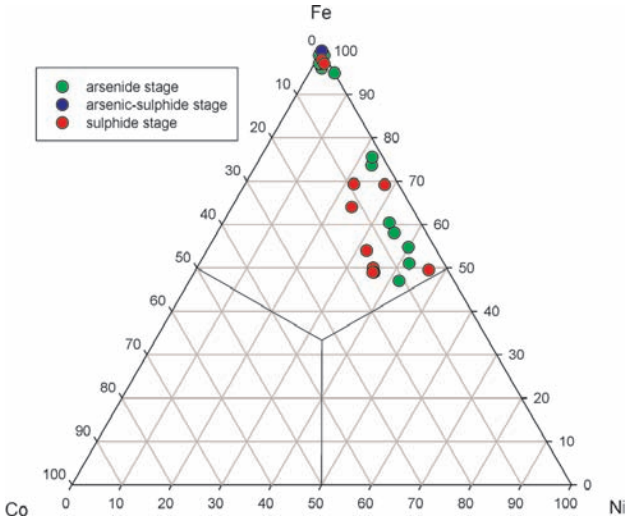

Fig. 69. Ni–Co–Fe ratio (atomic values) in pyrite of selected mineralization stages

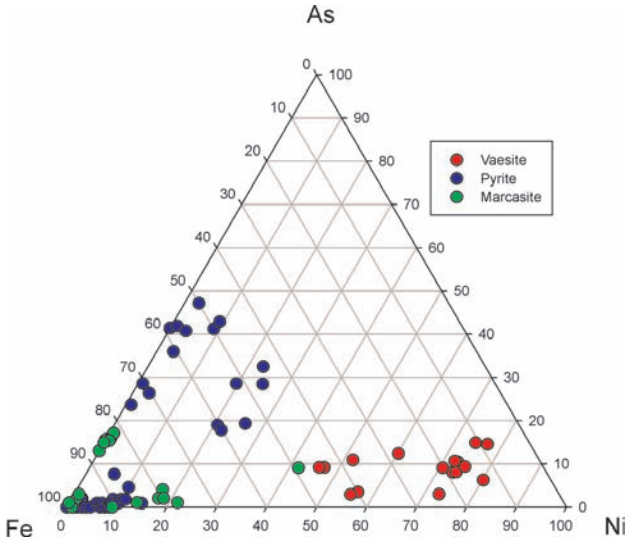

Fig. 70. Fe–Ni–As ratio (atomic values) in pyrite, marcasite, and vaesite.

Group of tetrahedrite–tennantite *(tennantite, tetrahedrite, argentotennantite, freibergite)*

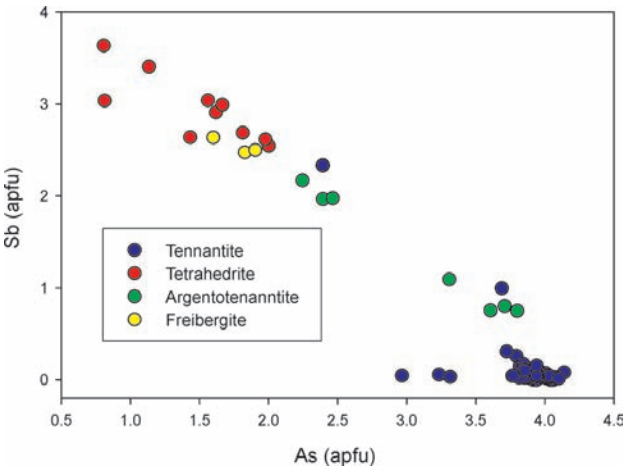

Fig. 71. Sb (apfu) vs. As (apfu) diagram for tetrahedrite group minerals.

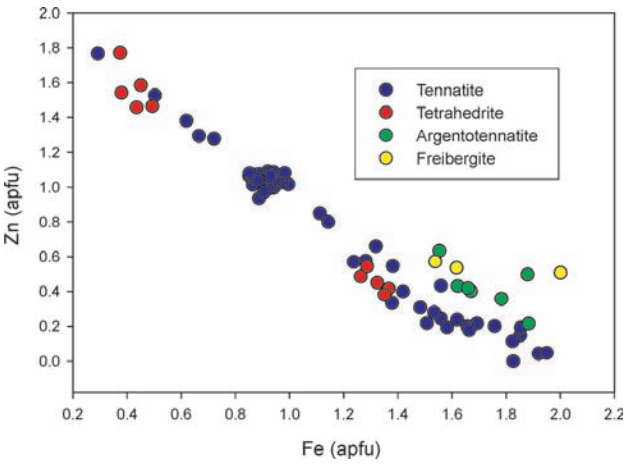

Fig. 72. Zn (apfu) vs. Fe (apfu) diagram for tetrahedrite group minerals. Argentotennantite and freibergite are Fe dominant members; two types (Fe and Zn dominant) of tetrahedrite are observed and Fe–Zn solid solution in tennantite was found.

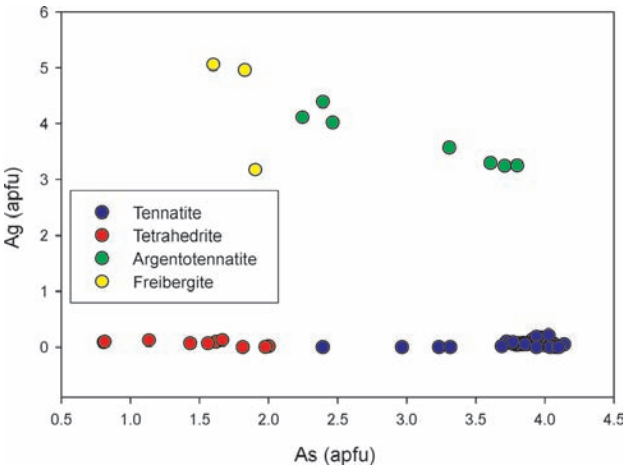

Fig. 73. Ag (apfu) vs. As (apfu) diagram for tetrahedrite group minerals. The minerals are separated into two group – Ag-free and Ag-rich; no intermediate member was found.

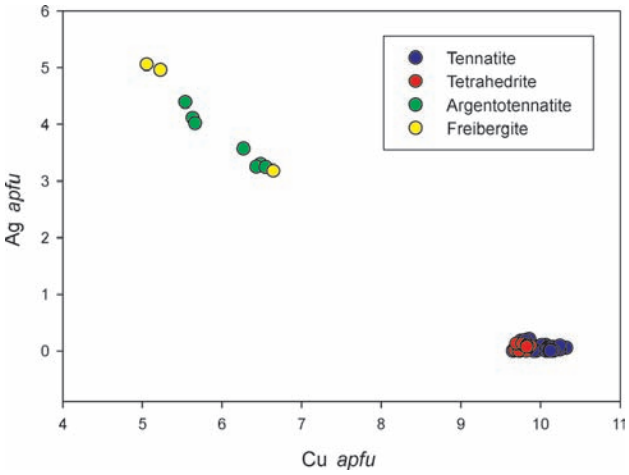

Fig. 74. Ag (apfu) vs. Cu (apfu) diagram for tetrahedrite group minerals. There are two groups of analyses: Ag-free tennantites and tetrahedrites and Ag-rich (in the range 3–5 Ag *apfu*) freibergites and argentotennantites.

DEDUCING THE CONDITIONS OF FORMATION OF SELECTED SULPHIDES

The Jáchymov ore veins represent a multicomponent natural ore system. Individual stages of its development differ in their age, chemistry and p–T conditions. Furthermore, the p–T conditions varied within the individual mineralization stages, and the mineralizations formed during different stages overlap in space. Consequently, it is often difficult to assign individual minerals to a specific mineralization stage. In the ore assemblages studied, disequilibria are very common, as is manifested by the occurrence of zoned crystals, reaction rims, colloform structures and the presence of various metastable assemblages. A low-temperature re-equilibration of higher-temperature ore assemblages is visible in exsolution intergrowths. Likewise, a change in the chemistry of ore-bearing fluids is preserved in the form of replacement textures. All of these effects make the estimation of the p–T conditions of formation a difficult task.

Sn–W sulpharsenide stage

This is a high-temperature stage related to the processes of greisenization of the granite that underlies the Jáchymov ore district. *Chalcopyrite*, *stannite*, *sphalerite*, *kësterite*, and *roquesite* formed broad solid solutions under the (high) temperatures that prevailed during their primary crystallization that, in turn, gave rise to typical breakdown textures formed during a subsequent period of cooling. Unfortunately, low-temperature solvi in the corresponding synthetic systems have not been studied. Nevertheless, the presence of *mawsonite* in this mineralization stage indicates that the temperature of formation could not have exceeded 390 °C. Considering also other evidence, the temperature of formation of minerals in this stage can be estimated at ~300 °C. Frequent intergrowths of *stannite* with *mawsonite* demonstrate that these minerals form a stable association. This is in agreement with [514] but it is difficult to reconcile with the observation of [510] who described the association of *stannoidite* with *stannite* as a stable one. The occurrence of *cassiterite* in this mineral assemblage indicates a higher activity of O_2 during this stage.

Arsenide stage

This stage is characterized by the presence of native Ag, Bi (Hg) and of Co–Ni(Fe) arsenides and sulpharsenides. According to the presence of either *silver* or *bismuth*, this stage is further subdivided into silver and bismuth parageneses. The presence of native metals proves a very low activity of sulphur, certainly below that of the univariant sulphidation curves of Ag/Ag_2S, Bi/Bi_2S_3 and Hg/HgS. The observed succession of Co–Ni(Fe) arsenides ⇒ diarsenides ⇒ triarsenides corresponds to a gradually increasing activity of arsenic during this stage. The appearance of *bismuthinite* and *bornite* in the late phases of the *arsenide* stage documents an increasing sulphur activity, above that of the univariant curves *bismuthinite*/*bismuth* and *bornite*+*pyrite*/*chalcopyrite*. Also, the presence of younger sulpharsenides with elevated contents of sulphur indicate a higher activity of sulphur in the later phases of this stage. For example, sulphur contents in the studied *rammelsbergite* are higher than the maximum content (1 wt. %) determined experimentally by [490], and vary within the range of 0.02–19 wt. % whereas in *pararammelsbergite*, the sulphur contents reach only 0.08–2 wt. %. The analyses also point out the unexpected existence of a *rammelsbergite–gersdorffite* isomorphous series. The existence of the same solid solution has recently been reported by Fanlo et al. [587] from the San Juan de Plan deposits in Spain. The variation in the As/S ratio in *gersdorffite* and *rammelsbergite*, also echoed in *arsenopyrite*, reflects the variation in sulphur activity during their formation. Unfortunately, no experimental data are available and therefore it is not possible to use the As/S ratio of *gersdorffite* and *rammelsbergite* (and *arsenopyrite*, [503]) as a geothermometer. Fortunately, the occurrence of skeletal aggregates of *bismuth* crystals can be used as a fixed-point geothermometer; the crystals must have grown below the melting point of Bi (271 °C). Likewise, the occurrence of *argentite* indicates a temperature above 179 °C. *Rammelsbergite* is an interesting mineral, because it is stable above 590 °C and inverts to *pararammelsbergite* at lower temperatures. However, any temperatures near 590 °C appear unacceptably high, but it should not be forgotten that the possible effect of the activity of sulphur on the temperature of this phase transition remains unknown. Still, this disqualifies *rammelsbergite* from the arsenic stage as a fixed-point geothermometer. Karup-Møller and Makovicky [395] pointed out a topotactic influence of the matrix on the

crystallization of *rammelsbergite*. Consequently, we can only roughly estimate the temperature of formation as being below 300 °C. Roseboom [512] studied the pseudoternary system of $NiAs_2$–$CoAs_2$–$FeAs_2$ and reported a wide solid solution with a miscibility gap between $NiAs_2$ and $FeAs_2$. This miscibility gap corresponds to the analyses of diarsenides from Jáchymov. Again, no experimental data exist on the low-temperature solvi in this system that would allow us to narrow down the possible range of temperature.

Arsenic–sulphide stage

In this stage, the sulphur activity varied very widely. Native metals are represented by *arsenic*, dendritic aggregates of *silver*, native *antimony*, and intermetallic alloys *dyscrasite*, AsSb and BiSb. Native *silver* and *antimony* indicate a sulphur fugacity below that of the *argentite*/*silver* and *stibnite*/*antimony* univariant curves (Fig. 44). On the contrary, minerals such as *realgar* (stable below 265 °C [507]), *proustite* and *robinsonite* together with a sulphur-rich *rammelsbegite* and *safflorite* indicate that the sulphur activity must have been above that of the *pyrite*/*pyrrhotite* univariant curve (Fig. 44). Also, several sulphides are present that have a limited field of thermal stability and thus could be used as fixed-point geothermometers. *Xanthoconite* is stable at up to 191 °C, and transforms to the high-temperature phase of *proustite* above this temperature. *Stromeyerite* is stable at temperatures below 93 °C, whereas the presence of *argentite* and *pyrargyrite* indicates temperatures of formation above 197 °C [506] and 192 °C, respectively [444]. In addition to that, *stenbergite* has a narrow field of thermal stability and breaks down at 152 °C to *argentite*, *pyrite* and *pyrrhotite* [445], [508]. *Proustite* and *pyrargyrite* form a complete solid solution at above 300 °C, but have a miscibility gap at lower temperatures [513], [347]. The lamellar intergrowths of *pyrargyrite* and *proustite* thus indicate temperatures of formation below this temperature, even though the relevant solvi remain unknown. All these fixed-point geothermometers indicate low temperatures of formation, probably in the range of 100–200 °C.

Sulphide stage

In the *sulphide* stage, the main minerals are simple sulphides: *chalcopyrite*, *sphalerite*, *galena*, *pyrite*, accompanied by sulphosalt *robinsonite*. *Löllingite, tennantite* and arsenian *pyrite* are the principal bearers of arsenic in the stage. The broad stability fields of these minerals do not permit to use these minerals as fixed-point geothermometers. Only the presence of *bornite* with exsolution intergrowths of *chalcopyrite* indicates a higher temperature of formation which, unfortunately, cannot be quantified any closer. Low-temperature Cu (Fe) sulphides with narrow fields of thermal stability represent late phases of the *sulphide* stage. These minerals indicate temperatures of formation below 100 °C. *Djurleite* breaks down at 93 °C, *anilite* at 87 °C [507], and *smythite* is reported to be stable below 75 °C [554]. The presence of sulphosalts is a consequence of a higher sulphur activity in this stage (Fig. 44). A very low iron content of *sphalerite* furnishes evidence of the high activity of sulphur during the crystallization (assuming a low pressure of formation and the presence of iron in the system).

Conclusions

The hydrothermal vein systems at Jáchymov were formed under a relatively low sulphur activity and at low temperatures – otherwise the mineral assemblages would contain no native metals and sulphides with a low thermal stability. During the late phases of individual mineralization stages, the sulphur activity increased and the temperature decreased. Sulphosalts and sulpharsenides started to crystallize in these late phases.

A feature common to all mineral assemblages is the low activity of oxygen: with the exception of *cassiterite* (in the *Sn–W sulpharsenide* stage), no metal oxides are present in the studied ore assemblages.

PARAGENETIC RELATION OF PRIMARY AND SECONDARY MINERALS

Compared to secondary minerals of the Jáchymov ore district, its primary mineralization is fairly simple in its ore minerals as well as gangue minerals. Combinations of major primary minerals occur practically in the whole vertical range of the veins. However, this is not exactly valid for all veins and in the whole district [475], [476], [477].

A typical scheme of a vein deposit with a leached oxidation zone, enriched oxidation zone, and cementation zone above unchanged primary zone, is seen only on Geister and Geschieber veins and partly also on the Červené veins, which reach up to the surface. Majority of accessible surface outcrops of other veins show a relatively small zone of nearly complete leaching of ore components, with only sporadic occurrences of secondary uranium minerals (particularly *torbernite*, *autunite* and also *uranophane* and *kasolite*), bismuth minerals (*bismutite*, *bismutoferrite*), copper (*malachite*, *mixite*) and lead minerals (*anglesite*, *pyromorphite*). Even the relatively limited accumulations of secondary minerals may be leached, as indicated by limonite pseudomorphs after uranium micas. Majority of the veins do not crop out on the surface. Upper parts of veins were removed by erosion and only middle and lower parts of veins remained.

The enriched cementation zone exploited in 16th century contained mainly *silver*, *acanthite* and *chlorargyrite*. As noted by Mathesius [308], the richest accumulations of ores were located at a depth of 60–80 m. The fact that *uraninite* reputedly occurred mainly at lower levels may be due to its better solubility in the descending meteoritic water during supergene evolution.

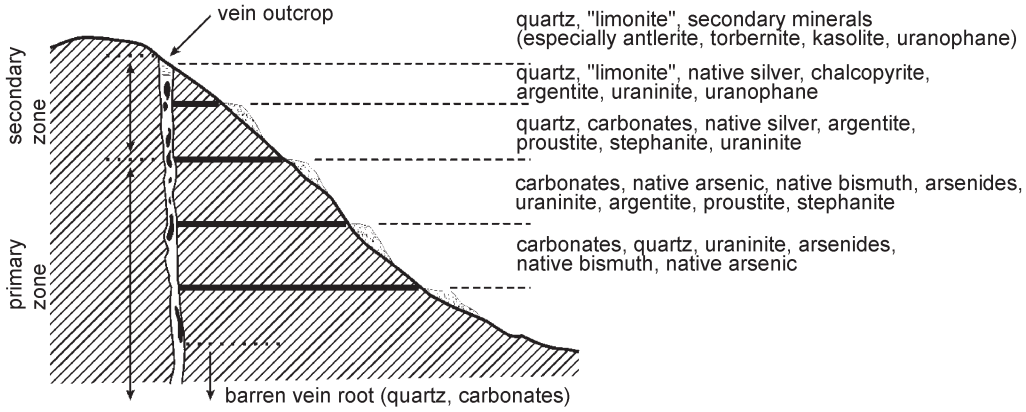

Fig. 75. Schematic vertical distribution of the *five-element* formation (Ag–Bi–Co–Ni±U) in a midnight vein.

A weak limonitization was limited to parts of veins immediately reaching the land surface.

The richest secondary mineral assemblage formed under the recent or historically imposed conditions. The occurrence of the same or similar secondary minerals depends mainly on the content of the ore vein. This trend is seen nearly in the whole vertical range of the veins. The quantity of circulating "fracture" water and the mode of exposure of the ore vein by mining play the main role. Subrecent minerals formed as a result of long-lasting mining activity.

Weathering processes induced by mining activity

Underground exposures of massive ores (including *bismuth*, *nickel-skutterudite*, *pyrite*, *arsenic* and *uraninite*) carry minor coating of powdery secondary minerals. Rich occurrences of recently formed secondary minerals were found in places where the ore was widely dispersed by explosions. Rich accumulations of secondary minerals were found in parts of ore-free adits, where fine-grained part of ore from overturned tub was spilled on the floor (e.g., *lindackerite*, *geminite* at the 7th (Werner) level of the Rovnost I shaft). Rich accumulations of *zýkaite* were found on disintegrating mica schist containing *arsenopyrite*. Generally, occurrences of secondary uranium minerals are common in the proximity of water drainage "ditches" as coatings on barren rocks in adits, including minerals like *čejkaite* [473], [479], a.o.

Special objects include waste rock fill of exploited sections and pillars. Carbonate-rich gangue is easily dissolved, resulting in *calcite* and *aragonite* stalactite decorations in adits. The stalactites are often coloured in blue (Cu), violet to brown pink (Co), rusty (Fe), and most frequently yellow (U). In the Geschieber vein, *calcite* drapes 0.75 m long formed during the 20 years after mining was terminated. Besides *calcite* stalactites, stalactites of pure *znucalite* up to 3 cm long formed in the Evangelist vein. Up to 1 m long stalactites of muddy "*glockerite*" were observed at places with rich *pyrite*. Brown, rope-like accumulations of algae proliferating on rotting wood supports are impregnated and lapidified by infiltration of *calcite*.

Alteration of bismuth minerals

Secondary bismuth minerals do not accompany rich native *bismuth* accumulations associated with Ni and Co arsenides; their formation in historical times has not been observed. On the other hand, secondary Bi minerals formed where *bismuth* was dispersed as a minor component in the ores and particularly where *bismuth* was partly replaced by *bismuthinite*. Exceptionally, *bismuthinite* needles protruding to vugs in porous gangue are coated by a thin layer of *bismutite*, usually without other mineralization.

Alteration of arsenic

Massive *arsenic* aggregates are less susceptible to weathering than complex ores. *Arsenic* accumulations are locally covered by powdery *arsenolite* coatings and small *pharmacolite* crystals. Rather different behaviour has been noted with porous *arsenic* from the Geschieber vein. In addition to relatively abundant *arsenolite* and *claudetite* crystals, aggregates of strongly acidic *kaatialaite* occur here, with compact crusts of *scorodite* in their proximity. This type of *arsenic* contains disseminated *pyrite*, which on weathering accelerates the dissolution of *arsenic*. Some specimens of this type of *arsenic*, without *scorodite*, carry droplets of a strongly acidic liquid, which persists on these specimens for years, when stored in a dry environment. It is assumed that the drops are formed by hygroscopic arsenic acid. Other specimens of porous *arsenic* carry prisms filled inside with powdery sulphur and crust of *pyrite* or *acanthite*. These pseudomorphs are clearly after *argentopyrite*.

In the Geschieber vein, a vertical chimney penetrating lenses of native *arsenic* was used for draining water from an adit. In areas where water flowed on *arsenic*, dendritic *silver* precipitated. As the place is no more accessible, it is uncertain whether *silver* precipitated from flowing mine water containing Ag^+ ions or from leaching minor *proustite* disseminated in *arsenic*. *Silver* dendrites were up to 1 cm long, they precipitated within 10 years after this place was mined in 1962 (samples were collected here in 1972–1973).

Alteration of arsenides, sulpharsenides and sulphides

The 12th level of the Svornost mine exposed strongly crushed and weathered Geschieber vein without noticeable mineralization with rich water supply, accompanied by recent growth of *köttigite* crystals, almost on day-to-day basis.

In the proximity of borehole HG-1, near the contact of granite with metamorphic mantle, the discharge of the Běhounek radioactive spring, in places with massive ores, is accompanied by a rich assemblage of secondary minerals, mainly sulphates. It includes *nickelhexahydrite*, *morenosite*, *jarosite*, *arsenolite*, *kaatialaite*, *švenekite*, crusts of magnesian *annabergite*, and extremely rare minerals *vajdakite* [472] and *cobaltkoritnigite*. Highly acidic minerals such as *kaatialaite* and *švenekite*, acidic as well as basic minerals (*jarosites*, *copiapite*) occur here in close proximity. Sulphates of vitriol type co-occur with arsenates *krautite*, *rösslerite*, a.o. Cations include nearly all ore components (Ni, Co, Zn, Fe), as well as cations derived from carbonate gangue and from wall-rocks: Ca, Mg, Mn, and Al, and cations brought by the radioactive thermal spring (Na, K). The ultimate source of molybdenum contained in *vajdakite* has not been identified, and possibly comes from the altered younger granite. Surprisingly, the deepest levels in the mine thus abound with minerals of oxidation zone, including native copper. So far, no secondary minerals of silver and lead have been encountered. *Jarosite* formed in the proximity of strongly corroded *proustite* crystals, but *argentojarosite* or native *silver* are absent. It is possible that *silver* was removed in the form of soluble silver sulphate or arsenate.

Alteration of pyrite and marcasite

Marcasite weathers more readily than *pyrite*. *Marcasite* decomposition, accompanied by the formation of sulphuric acid, acts as a catalyst, as it triggers and accelerates *pyrite* decomposition. In the absence of other components, alteration of *marcasite* and *pyrite* started by reaction of FeS_2 with oxygen from air in the presence of water (even air humidity). Sulphur changed its oxidation state. Where the alteration proceeded slowly, some powdery sulphur may coat corroded sulphides. In case of spontaneous reactions, sulphur quantitatively acquires oxidation state VI. This process is accompanied by an increase in the volume of sulphide aggregates, fracturing and coating by rusty films of amorphous ferric sulphates. If hydrolysis of these products sets in, and if pH of the solution increases above 4.5, ferric ion is precipitated in the form of complex hydro-sulphates. Sulphuric acid released by this reaction accelerates weathering of additional FeS_2 and carbonates. Large volumes of FeS_2 resulted in Fe^{2+} and SO_4^{2-} concentrations exceeding solubility, and skeletal aggregates of vitriols – sulphates crystallized on the surface of the sulphides. The presence of *gypsum* also serves as an indicator of conditions suitable for the crystallization of secondary sulphates.

Alteration of Cu minerals

Interesting is also the occurrence of copper minerals at the Daniel level, at the intersection of the Trojická vein and Geschieber vein. A *quartz* lens penetrated by carbonate veinlets contains primary *pyrite*, *bornite* and *tennantite*. Copper arsenates *lindackerite*, *geminite*, *lavendulan*, *strashimirite* and other unknown Cu-arsenate species [474] formed in the proximity of primary copper minerals. Nearby porous *arsenic* was accompanied by common arsenates of Ca and Mg. However, fragments of *arsenic*, mixed with relics of Cu minerals possibly in the process of mining, yielded copper arsenates (*geminite*, *lindackerite*).

The Geister vein between the 3rd and 7th levels (Albrecht) of the Rovnost I mine yielded accumulations of newly formed cementation copper. A chimney between the levels, functioning as a water channel, exposed coatings of hydrated iron oxides and arborescent and flaky copper aggregates on all iron and wooden constructions.

Alteration of U minerals

As a general rule, the least developed secondary mineralization occurs in the proximity of carbonate veins. Primary minerals including *uraninite* are nearly unaffected by the alteration. Minor coatings of Ca and Mg arsenates and local coatings of uranium carbonates (*liebigite*, *schröckingerite*, *zellerite*) were formed. Vein carbonates with *uraninite* found in dumps are usually preserved rather fresh. In the presence of significant *pyrite*, the surface of the samples was corroded but secondary mineralization was limited to an amorphous glassy yellow coating in the proximity of *uraninite*. Massive *uraninite* in *quartz* veins or *uraninite* veins in the country rock is weakly weathered to *zippeite* or *uranopilite*, depending on the amount of *pyrite*. If arsenide was present in the vein, the most common weathering product was *(meta)zeunerite*. In the presence of very abundant *pyrite*, *uraninite* was coated by a thick limonitic crust and no secondary minerals were formed.

A different situation exists in the wet environment in the mine. *Uraninite* accompanied by *pyrite* is strongly weathered, coated by *zippeite* and *uranopilite*. A different situation occurs with the carbonates. Secondary uranium minerals are sometimes deposited at a distance from *uraninite* without obvious reason or relation to any other mineralization. Dusted walls of adits, representing surfaces with efficient evaporation, represent a favourite site for the crystallization of secondary uranium minerals. A similar role is played by pieces of rock lying on the floor, particularly in the proximity of drainage ditches. Walls of adits may be covered with small aggregates of *schröckingerite* on areas of several square meters.

Weathering of *uraninite* is critically dependent on the character of the environment. It is nearly insoluble under reducing conditions or alters to *coffinite* [150], but is unstable under oxidation conditions; the efficiency of alteration is notably increased in the presence of water.

In dry environment, *uraninite* is subject to oxidation by oxygen diffusion into interstitial structural sites. Owing to the presence of other elements than uranium, an ideal UO_2 cubic structure of the *fluorite* type is not materialized. Limits for oxidation occur with the value x = 0.25, characterized by a shift in unit-cell parameters, while cubic structure is retained $UO_{2.25}$, i.e., U_4O_9) and at x = 0.33, resulting in a distortion of cubic structure to body-centred distorted tetragonal structure $UO_{2.33}$ (U_3O_7) [471]. These changes may result in weakened coherency of granular aggregates, formation of microfractures and increase in the reactive surface of the material.

Progressive oxidation toward U_3O_8 ($UO_{2.67}$) is accompanied by the transformation of tetragonal structure to orthorhombic, which is associated with a significant volume change. However, this transformation takes place only at temperatures above 150 °C [458].

In the presence of water (or wet air), changes in uranium oxidation do not exceed $UO_{2.33}$, since dissolution sets in under these slightly oxidative conditions. Oxidation of *uraninite* in water-rich environment is characterized by more efficient kinetics compared to the alteration in air. Its alteration and dissolution leads to the formation of phases containing U^{6+} in the form of very stable UO_2^{2+}.

Factors controlling *uraninite* destruction include temperature, pH, oxygen fugacity, and concentration of ions such as SiO_4^{4-}, HCO_3^-, HSO_4^- $H_2AsO_4^-$, and Ca^{2+}, admixtures, grain size, presence of other minerals, especially *pyrite*, and others.

Interesting information on underground weathering of ore components was revealed in the historic Giftkiesstollen. These old workings were penetrated during the 1950s by new works in the course of uranium mining (*Jáchymovské doly* enterprise). The breccia resulting from old historic mining, comprising fragments of *uraninite*, *pyrite*, *chalcopyrite* and gangue minerals (*quartz*, *dolomite*, *calcite*), was cemented by *gypsum*, *jarosite*, *plumbojarosite* and a number of uranium minerals (oxyhydroxides, silicates, sulphates, carbonates).

Newly formed products resulting from *uraninite* decomposition show a certain sequence of precipitation. This was made possible by the fact that large amounts of finely crushed ore fragments remained on the spot after a blast in the course of mining operation. Crushed ore included abundant *uraninite* in grains 2–5 mm in size. The effective surface of this material was large and contributed to effective weathering. This material was not drained by water and was exposed to air with certain moisture. *Uraninite* in this artificial breccia was grey to bluish grey, with matt powdery to porous surface, free of secondary uranium minerals, although they were present in the proximity. Secondary minerals concentrated mainly in the proximity of gypsum.

The observed succession of crystallization of secondary minerals is as follows:

uraninite →
metaschoepite $(UO_2)_8O_2(OH)_{12}(H_2O)_{10}$,
schoepite $(UO_2)O_2(OH)_{12}(H_2O)_{12}$ →
becquerelite $Ca(UO_2)_6O_4(OH)_6(H_2O)_8$,
compreignacite $K_2(UO_2)_6O_4(OH)_6(H_2O)_7$ →
masuyite $Pb(UO_2)_3O_3(OH)_2(H_2O)_3$,
vandendriesscheite $Pb_{1.57}(UO_2)_{10}O_6(OH)_{11}(H_2O)_{11}$ →
uranophane $Ca(UO_2)_2(SiO_3OH)_2(H_2O)_5$,
sklodowskite $Mg(UO_2)_2(SiO_3OH)_2(H_2O)_6$,
cuprosklodowskite $Cu(UO_2)_2(SiO_3OH)_2(H_2O)_6$.

The interpreted precipitation of oxyhydroxides before silicates is supported by the observation of oxyhydroxides in some samples covered by silicates, mainly small spheres of *cuprosklodowskite*; a reversed sequence was not observed. Otherwise, the two groups of minerals tend to occur separately.

pyrite → *melanterite* + *gypsum*:

$$FeS_2 + 3.5O_2 + H_2O \rightarrow Fe^{2+} + 2SO_4^{2-} + 2H^+$$

typical way of *uraninite* oxidation:

$$UO_2 + 2H^+ + 1.5O_2 \rightarrow UO_2^{2+} + H_2O$$

and examples of hydrolysis of UO_2^{2+} ions and formation of basic uranium oxyhydroxides:

formation of *metaschoepite*:

$$8UO_2^{2+} + 16OH^- + 8H_2O \rightarrow (UO_20)_8O_2(OH)_{12}(H_2O)_{10}$$

formation of *schoepite*:

$$8UO_2^{2+} + 16OH^- + 10H_2O \rightarrow (UO_2)_8O_2(OH)_{12}(H_2O)_{12}$$

formation of *becquerelite*:

$$6UO_2^{2+} + Ca^{2+} + 14OH^- + 4H_2O \rightarrow Ca(UO_2)_6O_4(OH)_6(H_2O)_8$$

formation of *compreignacite*:

$$6UO_2^{2+} + 2K^+ + 14OH^- + 3H_2O \rightarrow K_2(UO_2)_6O_4(OH)_6(H_2O)_7$$

becquerelite → *uranophane*:

$$Ca(UO_2)_6O_4(OH)_6(H_2O)_8 + 6SiO_2 + 2Ca^{2+} + 4OH^- + 5H_2O \rightarrow 3Ca(UO_2)_2(SiO)_3(OH)_2(H_2O)_5$$

The strongest representation among newly formed minerals have oxyhydroxides of uranyl, forming spheroidal glassy aggregates or highly lustrous minute crystals. Uranium silicates are less abundant, occur in a powdery form, such as *uranophane* and *sklodowskite*, or form coatings and small radiating spheroidal aggregates

(cuprosklodowskite). These minerals constituted cement of the described "breccia".

The presence of other uranyl minerals was sporadic. They include phases which occur largely in the proximity of fragments representing the source of the respective ions. The carbonates *metazellerite* $Ca(UO_2)(CO_3)_2(H_2O)_3$ and *zellerite* $Ca(UO_2)(CO_3)_2(H_2O)_5$ concentrated always in the proximity of *dolomite* fragments, *metazeunerite* $Cu(UO_2)_2(AsO_4)_2(H_2O)_8$ near *chalcopyrite*. Sulphates do not show such dependence on the source. *Uranopilite* $(UO_2)_6(SO_4)(OH)_{10}(H_2O)_{12}$ is generally associated with *gypsum*. *Rabejacite* $Ca(UO_2)_4(SO_4)_2(OH)_6(H_2O)_6$ was found on earthy coating of larger rock fragments or around uranyl oxyhydroxides together with gypsum. The originally present *pyrite* fragments were probably completely decomposed. Other types of uranium minerals were not recorded in this particular assemblage, e.g., minerals of the *zippeite* group, common in other places, or other uranyl carbonates. The respective ore batch was obviously poor in carbonate gangue, and the relatively small amount of *pyrite* was consumed in *jarosite*- and *gypsum*-producing reactions. The lead contained in *plumbojarosite* is almost certainly of radiogenic origin, since no primary lead minerals were found.

Similar conditions of hydration-oxidation weathering of *uraninite* were recorded in upper levels of the Evangelista vein. The identified secondary minerals include oxyhydroxides (*metaschoepite*, *becquerelite*, *compreignacite*), silicates (*uranophane*, *sklodowskite*) as well as carbonates (*liebigite*, *schröckingerite*). Somewhat more common are uranyl-sulphates (*uranopilite*, *zippeite*, *johannite*) and *plumbojarosite* containing radiogenic lead. Common *jarosite* and *gypsum* also occur.

FLUID INCLUSION STUDY

Fluid inclusions in *barren* quartz, *fluorite* and carbonates of the *Sn–W sulpharsenide*, *arsenide, arsenic–sulphide* and *sulphide* stages of the vein Ni–Co–Bi–Ag±U mineralization were studied at Jáchymov. The results also comprise the data of Benešová (in [359]) on dark violet fluorite of the *carbonate–uraninite* stage.

Table 5. Results of fluid inclusions measurement from Jáchymov deposit.

sample	mineral	FI type	LVR	Th	Tm	salinity	Tfm	Ts	Tm CO_2
(mineralization stages)			(L/L+V)	(°C)	(°C)	(wt. %)	(°C)	(°C)	(°C)
Sn–W sulpharsenide stage									
J066P	quartz	prim	0.6	294–306	–19.6	20	–52.5		
	quartz	prim	L+V+S	246		35		264	
J107P	quartz	prim	0.2		–1.4	2.4			–56.5
	quartz	prim	L+V+S	210–218		33		240–246	
	quartz	prim	0.6		–4.8 to –6.2	7.6–9.5			
Trojická vein	quartz	prim	0.7	246–262	–4.6 to –5.0	7.3–7.9	–34		
Carbonate–uraninite stage									
dark violet fluorite [359]	fluorite	prim	0.9	190–198					
Arsenide stage									
J005I2	Fe-dolomite	prim	0.95	96–112	–25.8 to –29.2	23.5–24			
J006I	ankerite	prim	variable	118–142	–22.4 to –25	22–23	–55.8		
J007I	dolomite	prim	variable		–22.4 to –29.6	22–24	–54		
J008I1	red dolomite yellow	prim	0.9	118–140	–25.2	23			
J008I2	dolomite	prim	0.9	126–144	–22.6 to –30	22–24.5			
J019P	carbonate	prim	variable		–38	?			
J119P	carbonate	prim	0.95	112. 114	–8.9	12.7			
MP271D	carbonate	prim	variable		–0.2 to –0.5	0.4–0.9			
Arsenic–sulphide stage									
NM9527	Mg-calcite	prim	0.95	112–123					
J009I2	Fe-dolomite	prim	0.95	112–138	–24.5 to –25.7	23–23.5	–60		
J009I1	dolomite	prim	variable		–0.2	0.4			
Sulphide stage									
J004I	calcite	sec	0.95	70–80	–2.1 to –2.4	3.6–4.0			
	calcite	prim	L-only	< 100	–0.1 to –0.3	0.2–0.5			

temperature of homogenization (Th), temperature of the first melting (Tfm), temperature of melting of the last crystal of ice (Tm), temperature of melting of CO_2 (Tm CO_2), temperature of solid phase dissolution (Ts). L – liquid phase, V – gaseous phase, S – solid phase, FI type: prim – primary inclusions, sec – secondary inclusions.

Methods

A microthermometric study of the fluid inclusions was undertaken on doubly polished sections 300 mm thick and on cleaved carbonate chips. Fluid inclusions were analysed on a Chaixmeca heating-cooling stage [484], which was calibrated between 100 °C and 400 °C by Merck chemical standards, the solidification point of distilled water, and phase transitions in natural pure CO_2 inclusions. Homogenization and cryometric data show reproducibility of ±0.2 °C at temperatures below 0 °C and ±3 °C at temperatures to 400 °C.

Homogenization temperature (Th), temperature of first melting (Tfm) and of the final melting of ice (Tm), and temperature of melting of solid CO_2 (Tm CO_2) and temperature of dissolution of solid phase (Ts) were measured.

The salinity of the fluids was calculated according to Bodnar and Vityk [481] and the composition of the salt systems was determined according to Borisenko [482].

As *calcite*, *dolomite* and *ankerite* are cleavable minerals, fluid inclusions may change during subsequent evolution events and even during the preparation of the wafers and the microthermometric measurements ([480], [483]). Metastability, leakage, stretching and decrepitation of inclusions in these minerals can occur and have to be recognized and taken into account in the interpretation of the microthermometric data.

Results

Sn–W sulpharsenide stage

Primary aqueous inclusions in *quartz* of the J066P and J107P samples have a variable liquid-to-vapour ratio (LVR). Vapour-rich inclusions with LVR = 0.2 and liquid–vapour inclusions with LVR = 0.6 can be found. Moreover, L+V+S inclusions with NaCl daughter crystal and vapour bubble of about 30 vol. % were observed.

Very small amount of CO_2 was identified in vapour-rich inclusions. The temperature of melting of solid CO_2 was measured at –56.5 °C, which corresponds to the temperature of the triple point of pure CO_2. The salinity of vapour-rich inclusions is low, of about 2.5 wt. % NaCl equiv.

Homogenization temperatures of inclusions with LVR = 0.6 were measured between 294 and 306 °C. The salinity of these inclusions varies between 7.6 and 20 wt. % NaCl equiv., the salt system of the solution is formed by $CaCl_2$, NaCl, KCl, and probably $MgCl_2$ (Tfm = –52.5 °C).

The dissolution of NaCl daughter crystal in L+V+S inclusions was observed between 240 and 264 °C. The bulk salinity, estimated using Ts, is from 33 to 35 wt. %.

The relationships of these three fluid inclusion types are complicated; the preliminary data suggest that the inclusions represent a relatively high temperature–high salinity post-magmatic fluid.

Carbonate–uraninite stage

Benešová (in [359]) studied fluid inclusions in dark violet *fluorite*, which was sampled from U-rich mineralization. Primary aqueous fluid inclusions homogenized at temperatures between 190 and 198 °C. Pseudosecondary and secondary inclusions homogenized in the interval from 105 to 158 °C.

Arsenide stage

Fluid inclusions were studied in several carbonates of *dolomite–ankerite* composition (J005I2, J006I, J008I1, J008I2, J019P, J119P, and 217D). Primary inclusions of aqueous fluid have variable shape, size of max. 80 μm, and a variable liquid-to-vapour ratio. L-only, V-only, V>>L and L+V (LVR = 0.9 to 0.95) inclusions were found in 3D distribution. Variable LVR is believed to be caused by the long-term maturation of inclusions and nucleation of vapour phase under relatively low temperature [581]. Homogenization temperatures were measured in groups of the inclusions with LVR = 0.9 to 0.95 and ranged from 96 to 144 °C. Tm of ice was observed between –22.4 and –30 °C, and the bulk salinity of inclusions is between 22 and 24.5 wt. % (for H_2O–$CaCl_2$ salt system). Tfm was measured in the range from –54 to –55.8 °C and indicates a $CaCl_2$–NaCl–KCl±$MgCl_2$ salt system in the solution. Lower salinity was observed in the J119P sample, of about 13 wt. % NaCl equiv. and especially in the 271D sample, where the salinity of fluid in carbonate adjacent to *proustite* is very low, from 0.4 to 0.9 wt. % NaCl equiv.

Arsenic–sulphide stage

Primary H_2O inclusions in Mg-rich *calcite* of the NM 9527 sample show a consistent LVR = 0.95. The inclusions homogenized at temperatures between 112 and 123 °C. The shape of vapour bubble was deformed during cooling experiments, and the bubble obtained the original shape at temperatures of about +10 °C. This phenomenon is supposed to be caused by the formation and melting of clathrates of hydrocarbons. Thus, the vapour bubble probably contains a very small amount of hydrocarbons.

Primary H_2O inclusions with variable LVR (L-only, V>>L, L+V inclusions) were found in Fe-rich *dolomite* (sample J009I2). Homogenization temperatures were measured in L+V inclusions with LVR = 0.95 between 112 and 138 °C. The salinity of inclusions is high, of about 23 wt. %. Tfm = –60 °C and indicates the dominant portion of $CaCl_2$ in the solution.

The later *dolomite* of the J009I1 sample forms the hem on the older *dolomite*. Primary H_2O inclusions in this *dolomite* show a variable LVR and, in contrast, very low salinity, of about 0.4 wt. % NaCl equiv.

Sulphide stage

Calcite of the J004I sample contains primary H_2O inclusions. The inclusions are liquid-only and indicate low temperature of trapping of the inclusions, below 100 °C. The salinity of primary inclusions is very low, from 0.2 to 0.5 wt. % NaCl equiv.

Secondary H_2O inclusions along healed microfractures showed a consistent LVR = 0.95 and homogenized at temperatures between 70 and 80 °C. The salinity of secondary inclusions is low, from 3.6 to 4 wt. % NaCl equiv.

Discussion

The character of fluid inclusions in minerals of various paragenetic stages of the Jáchymov deposit indicates a long-term evolution of the hydrothermal system. The first generation of veins connected with the *Sn–W sulpharsenide* mineralization opened during early post-magmatic stage. *Carbonate–uraninite*, *arsenide*, *arsenic–sulphide,* and *sulphide* mineralization stages can be recognized during periodical opening of the veins under lower pT conditions. The high salinity of fluids suggests a deep circulation of ore-bearing fluids. The latest vein minerals formed under temperatures below 100 °C, from low salinity fluids.

Speaking about U-bearing mineralization, the obtained data can be compared with the results of fluid inclusion study from the Příbram and Rožná uranium deposits. Water-rich fluid inclusions from K3 and K5 calcite of the Příbram U deposit [582] showed Th between 62 and 131 °C and a low salinity, which does not reach 5 wt. % NaCl equiv.

Carbonates K4 of the U-bearing stage from the Rožná uranium deposit [583] have Th from 150 to 180 °C and the salinity of fluids up to 15 wt. % NaCl equiv.

The introduced temperature intervals of the formation of U mineralization correspond very well to the data of Poty and Pagel [584]. They suggested that most U-bearing mineralizations throughout the world formed under temperatures in the interval of 90 to 250 °C.

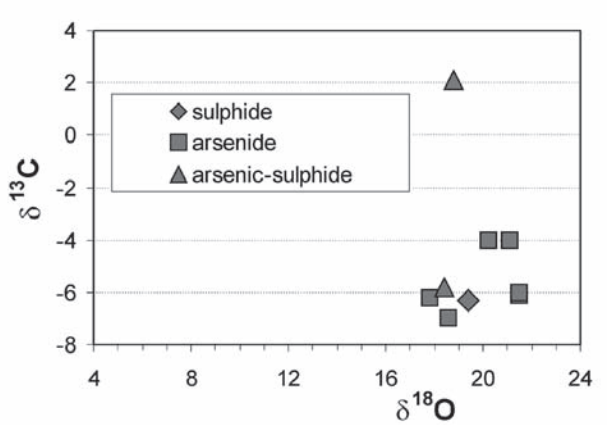

Fig. 76. $\delta^{13}C$ vs. $\delta^{18}O$ in carbonates of hydrothermal veins of the Jáchymov ore district.

STABLE ISOTOPES

Nine samples of carbonate [343] were analysed (see Table 6 and Fig. 76). Isotope data of oxygen and carbon are in most cases homogeneous, which indicates relatively uniform source of carbon and water in the hydrothermal process and also stable physical-chemical conditions during the formation of carbonates, especially a limited variation in temperature.

Carbon of hydrothermal solution had calculated isotopic composition of about –6 to –8 ‰ PDB. According to Robinson [486], the supposed temperature of the formation of carbonates is 150 °C. Carbon with such isotopic composition may be mantle-derived or may represent the so-called homogenized carbon of the Earth's crust. Carbon of sample J009I1 originated probably from marbles which occur around the deposit, and from which the carbon was mobilized during the hydrothermal processes. Carbonate J009I1 forms white thin rhombohedral crystals in vugs. It is the youngest carbonate on the sample, i.e., it is younger than carbonate J009I2.

Calculated isotopic composition of oxygen of water in the hydrothermal solution was about +5 to +6 ‰ SMOW (according O'Neil et. al. [588]; supposed temperature of the formation of carbonates is 150 °C). Such water may

Table 6. Isotopic composition of O and C (‰) in carbonates of different mineralization stages of hydrotermal veins in the Jáchymov ore district.

sample	pt.	mineral	$\delta^{13}C$ PDB	$\delta^{18}O$ PDB	$\delta^{18}O$ SMOW	stage
J004I	1	calcite	–6.3	–11.1	19.4	*sulphide*
J005I	1		–6.2	–12.6	17.8	*arsenide*
J005I	2	Fe-dolomite	–4.0	–10.3	20.2	*arsenide*
J006I	1	ankerite	–7.0	–11.9	18.6	*arsenide*
J007I	1	dolomite	–4.0	–9.5	21.1	*arsenide*
J008I	1	dolomite	–6.1	–9.1	21.5	*arsenide*
J008I	2	dolomite	–6.0	–9.1	21.5	*arsenide*
J009I	1	dolomite	2.1	–11.7	18.8	*arsenic-sulphide*
J009I	2	Fe-dolomite	–5.8	–12.1	18.4	*arsenic-sulphide*

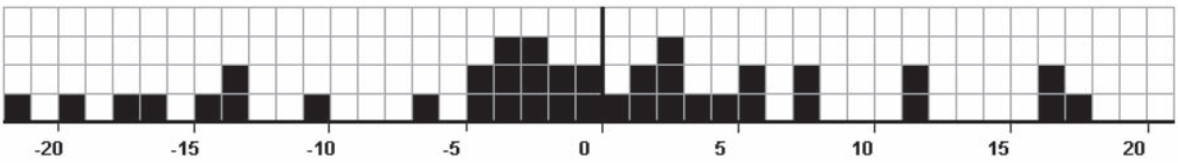

Fig. 77. Distribution of δS^{34} (‰ CDT) in sulphides from Jáchymov and surroundings according to [342].

be most probably either magmatic or metamorphic water, i.e., water isotopically equilibrated with metamorphic or igneous rocks at high temperature.

According to the data in [342], δ^{34} S values range from ca. –21 to +17 ‰ CDT – see Fig. 77. The lack of information on mineral species and mineralization stage of the respective samples analysed for S isotopes precludes a detailed interpretation.

Significant fluctuation in δ^{34} S values indicates changes in the source of sulphur of hydrothermal solution and/or (more probably) indicates changes in the physical-chemical conditions during the crystallization of sulphides (mainly pH, Eh, oxygen fugacity, sulphur fugacity).

As isotopic equilibrium among sulphides was not attained, the δ^{34} values cannot be used for thermometric calculations.

Rudotvorné procesy a minerální pragenze jáchymovského rudního okrsku

Práce charakterizuje hydrotermální žilný systém tzv. „pětiprvkové“ Ag–Ni–Co-Bi±U formace. Diskutovány jsou odlišnosti geneze U-formace a Ag–Ni–Co–Bi–As formace. Na základě rozdílného fyzikálně-chemického chování prvků Ag–Ni–Co–Bi–As je navržen model prvkové frakcionace hlubinných hydrotermálních zdrojů. Je diskutována role arsinu (AsH_3) pro mobilitu triády prvku Ni–Co–Fe. Je navrženo nové schéma mineralizačních stádií zohledňující tři rozdílné mineralizační zdroje. Je navržena nová geochemická interpretace hydrotermálních procesů jednotlivých mineralizačních stádií včetně detailní diskuse termodynamických podmínek mobility U^{VI} a precipitace uraninitu. Dále jsou detailně diskutovány podmínky krystalizace Ag a Bi dendritů, precipitace Ni–Co–Fe polyarsenidů a elektrochemické rozpouštění Ag. Jsou počítány termodynamické charakteristiky pro predikci a interpretaci geneze vzniku rudních minerálů ve vztahu k měnícím se Eh a pH podmínkám. V článku jsou uvedeny grafické interpretace chemických analýz, prvkových korelací a trendů pro vybrané minerály. Dále je korelován vznik sekundárních minerálů s přítomností primárních minerálů. Rovněž jsou studovány závislosti zvětrávacích procesů v souvislosti s důlní činností. Pro interpretaci rudotvorných procesů jsou uvedena data z měření fluidních mikroinkluzí a stabilních izotopů.